Biomedicine & Pharmacotherapy 161 (2023) 114520

Contents lists available at ScienceDirect

Biomedicine & Pharmacotherapy

journal homepage: www.elsevier.com/locate/biopha

Multimodal study of CHI3L1 inhibition and its effect on angiogenesis, migration, immune response and refractive index of cellular structures in glioblastoma

Agnieszka Rusak [a,*], Igor Buzalewicz [b], Monika Mrozowska [a], Benita Wiatrak [c], Katarzyna Haczkiewicz-Leśniak [e], Mateusz Olbromski [a], Alicja Kmiecik [a], Edward Krzyżak [d], Aleksandra Pietrowska [b], Jakub Moskal [f], Marzenna Podhorska-Okołów [e], Halina Podbielska [b], Piotr Dzięgiel [a,g]

[a] Division of Histology and Embryology, Department of Human Morphology and Embryology, Faculty of Medicine, Wroclaw Medical University, T. Chalubinskiego 6a St., 50-368 Wroclaw, Poland
[b] Department of Biomedical Engineering, Faculty of Fundamental Problems of Technology, Wroclaw University of Science and Technology, 27 Wybrzeze S. Wyspianskiego St., 50-370 Wroclaw, Poland
[c] Department of Pharmacology, Faculty of Medicine, J. Mikulicza-Radeckiego 2 Street, 50-345 Wroclaw, Poland
[d] Department of Basic Chemical Sciences, Faculty of Pharmacy, Wroclaw Medical University, Borowska 211A St., 50-556 Wroclaw, Poland
[e] Department of Ultrastructural Research, Faculty of Medicine, Wroclaw Medical University, T. Chalubinskiego 6a St, 50-368 Wroclaw, Poland
[f] Department of Neurosurgery, Poznan University of Medical Sciences, S. Przybyszewskiego 49 St., 60-355 Poznan, Poland
[g] Department of Physiotherapy, University School of Physical Education, I. Paderewskiego 35 Al., 51-612 Wroclaw, Poland

ARTICLE INFO

Keywords:
CHI3L1 inhibition
G721-0282
U-87 MG
Glioblastoma
Angiogenesis

ABSTRACT

Glioblastoma is one of the most aggressive tumours with a poor response to treatment and a poor prognosis for patients. One of the proteins expressed in glioblastoma tissue is CHI3L1 (YKL-40), which is upregulated and known for its angiogenesis-supporting and pro-tumour immunomodulatory effects in a variety of cancers. In this paper we present the anti-angiogenic, anti-migratory and immunomodulatory effects of the compound G721–0282, an inhibitor of CHI3L1. The inhibitor-induced changes were investigated using conventional techniques as well as the novel label-free digital holographic tomography (DHT), a quantitative phase imaging technique that allows the reconstruction of the refractive index (RI), which is used as an image contrast for 3D visualisation of living cells. DHT allowed digital staining of individual cells and intercellular structures based only on their specific RI. Quantitative spatially resolved analysis of the RI data shows that the concentration of G721–0282 leads to significant changes in the density of cells and their intracellular structures (in particular the cytoplasm and nucleus), in the volume of lipid droplets and in protein concentrations. Studies in the U-87 MG glioblastoma cell line, THP-1 monocytes differentiated into macrophages, human microvascular endothelial cells (HMEC-1) and in the spheroid model of glioblastoma composed of U-87 MG, HMEC-1 and macrophages suggest that inhibition of CHI3L1 may have potential in the antitumour treatment of glioblastoma. In this paper, we also propose a spheroid model for in vitro studies that mimics this type of tumour.

Abbreviations: CHI3L1, chitinase-3-like 1 protein; GBM, glioblastoma multiforme; VEGF, vascular endothelial growth factor; BBB, blood-brain barrier; MAPK, mitogen activated protein kinase; FAK, focal adhesion kinase; PI3K, phosphoinositide 3-kinase; AKT, serine/threonine-specific protein kinases;protein kinase B.

* Corresponding author.
E-mail addresses: agnieszka.rusak@umw.edu.pl (A. Rusak), igor.buzalewicz@pwr.edu.pl (I. Buzalewicz), monika.mrozowska@umw.edu.pl (M. Mrozowska), benita.wiatrak@umw.edu.pl (B. Wiatrak), katarzyna.haczkiewicz-lesniak@umw.edu.pl (K. Haczkiewicz-Leśniak), mateusz.olbromski@umw.edu.pl (M. Olbromski), alicja.kmiecik@umw.edu.pl (A. Kmiecik), edward.krzyzak@umw.edu.pl (E. Krzyżak), aleksandra.pietrowska@pwr.edu.pl (A. Pietrowska), nechisk2@ump.edu.pl (J. Moskal), marzenna.podhorska-okolow@umw.edu.pl (M. Podhorska-Okołów), halina.podbielska@pwr.edu.pl (H. Podbielska), piotr.dziegiel@umw.edu.pl (P. Dzięgiel).

https://doi.org/10.1016/j.biopha.2023.114520
Received 9 January 2023; Received in revised form 27 February 2023; Accepted 9 March 2023
Available online 13 March 2023

1. Introduction

Glioblastoma multiforme (GBM) is one of the most aggressive tumours, with only 8% of patients surviving 5 years after diagnosis [1]. The efficacy of therapeutic treatments, including surgical resection, radiotherapy and temozolomide administration, in some cases augmented by the use of bevacizumab, is limited by surgical resection options, high tumour heterogeneity, reduced drug delivery efficiency due to the blood-brain barrier (BBB), the so-called cold immunosuppressive microenvironment and tumour relapse caused by CD133 + cancer stem cells [1]. New therapeutic strategies, including poly (ADP-ribose) polymerase (PARP) inhibitors (veliparib), protein kinase inhibitors of PDGF, EGFR (erlotinib, gefitinib), VEGFR (cediranib) or FGFR, have insufficient therapeutic effect in the treatment of GBM and have mostly failed in clinical trials, as have sorafenib, imatinib, dasatinib, cabozantinib, the multi-target protein kinase inhibitors [1]. Therefore, targeted therapy in GBM remains a challenge. One of the proteins expressed in many types of cancer, including gliomas, and involved in angiogenesis, cell invasion, migration and immune response is the CHI3L1 protein [2–7]. The role of CHI3L1 in the angiogenesis that accompanies the neoplastic process has been demonstrated in in vitro studies and in vivo studies in a mouse model of human breast and colon cancer [3], [7]. CHI3L1 promotes angiogenesis by activating the MAPK/ERK and PI3K/AKT pathways in endothelial and glioma cells. This protein promotes the binding of syndecan-1 to integrin αvβ3 (in vascular endothelial cells) or integrin αvβ5 (in glioblastoma cells), which leads to the activation of FAK (Y861) and FAK (Y397) kinases (adhesion focal kinases) and consequently the MAPK/ERK and PI3K/AKT pathways [3], [7–9]. Studies in patient material have demonstrated the role of CHI3L1 in angiogenesis in breast cancer and glioma [7,10,11]. Importantly, few examples of inhibition of CHI3L1 expression in in vitro and in vivo breast cancer and glioma studies have successfully demonstrated its efficacy in inhibiting the angiogenesis process [3,7]. In this study, we focus on a CHI3L1 inhibitor, compound G721–0282, whose activity as a CHI3L1 inhibitor was first described by Park et al. [12].

The commercially available CHI3L1 inhibitor, compound G721–028, was selected using the SBVS (Structure-Based Virtual Screening) method, which consists in searching *in silico* for ligands or inhibitors for proteins and is applicable to the design of new drugs [13]. Thanks to the use of specific filters, this method makes it possible to search for molecules with suitable chemical and physical properties for drugs, characterising compounds that meet the criteria of oral bioavailability according to Lipinski's five rules [14]. Most, but not all, compounds with pharmacological or biological activity meet these criteria [13], [14]. Among the CHI3L1 inhibitors, which include K384–6111 [15], G721–0282 fulfils Lipinski's rule of five. In this study, we present a broad spectrum of influence of G721–0282 on glioblastoma U-87 MG cells and also on a spheroid model of brain tumours in in vitro culture. To the best of our knowledge, this is the first report on the effect of CHI3L1 inhibition by G721–0282 on glioblastoma cells and the first report on this type of spheroid containing glioblastoma, endothelial and also macrophage cells.

In addition, we have for the first time used the novel, non-contact, non-destructive and label-free digital holographic tomography (DHT) for the qualitative analysis of morphological changes within single cells exposed to the G721–0282 inhibitor under investigation. DHT has the potential to become an important diagnostic tool for the study of different biological samples: extracellular vesicles [16], eukaryotes [17–22] and prokaryotes [23–25], single cells or tissues [26]. By providing information on the 3D refractive index (RI) distribution of biological samples in relation to the concentration of intracellular chemical constituents in individual cells [20,27–30], it allows the qualitative examination of inhibitor-induced changes in morphology within individual cells as well as the quantitative analysis of induced changes in density, and intracellular structures (cytoplasm, nucleus/nucleoli and lipid droplets) caused by inhibitor-induced changes in intracellular protein within glioblastoma cells.

2. Materials and methods

2.1. G721-0282 inhibitor

he compound G721–028, with the IUPAC name 2-({6-butyl-1,3-dimethyl-2,4-dioxo-1 H,2 H,3 H,4 H-pyrido[2,3-*d*]pyrimidin-5-yl}sulfanyl)-N-(prop-2-en-1-yl)acetamide, was purchased from MolPort (compound number: MolPort-003–169–389 Mw=376. 48 g/mol, purity >90%) and was synthesised by ChemDiv, Inc (San Diego, CA, USA). The compound was resuspended in DMSO (dimethylsulphoxide) (Sigma-Aldrich, St. Louis, MO, USA) to a concentration of 100 mM [12] and this stock was further diluted in culture medium to the appropriate concentrations: 100, 50, 25, 12.5 and 6.25 μM.

2.2. Theoretical calculations on BBB permeation of G721-0282 compound

Theoretical calculations of the blood-brain barrier (BBB) permeation of compound G721–0282 were performed using *in silico* modelling. The distribution between blood and brain is a very important property for new drug candidates. Drugs that target the central nervous system must cross the blood-brain barrier to exert a therapeutic effect. Measuring blood-brain barrier penetration is typically difficult and costly. In the early stages of drug development, *in silico* prediction of BBB permeability is a good alternative. The most commonly used parameter to determine the ability to cross the blood-brain barrier is logBB=log (Cbrain/Cblood), where Cbrain and Cblood are the concentrations of the drug in the brain and blood, respectively. Based on different combinations of physicochemical parameters using QSAR analysis, many models have been proposed for the determination of logBB. Four of them were used to calculate the logBB of the compound studied. In the first model, the correlation between logBB and the logarithm of the octanol/water partition coefficient (log P) and molecular weight was used (Eq. 1, [31–33]). LogP was calculated using KOWWIN v1.68 (US EPA. [2012]. (Estimation Programs Interface Suite™, United States Environmental Protection Agency, Washington, DC, USA). Models 2–4 represent the linear free energy relationship (LFER) proposed by Abraham [34] - Eq. 2 [34], Eq. 3 [35], Eq. 4 [32]. Molecular descriptors: hydrogen bond acidity (A) and basicity (B), polarisability (S), molar refraction (E), McGowan volume (V) of a solute, were evaluated by PaDEL descriptor software [36].

$$\log BB = -0{\cdot}088 + 0{\cdot}272 \log P - 0{\cdot}001116 Mw \quad (1)$$

$$\log BB = 0{\cdot}044 + 0{\cdot}511E - 0{\cdot}886S - 0{\cdot}724A - 0{\cdot}666B + 0{\cdot}861\ V \quad (2)$$

$$\log BB = 0{\cdot}934 - 0{\cdot}743A - 0{\cdot}768B - 0{\cdot}605 + 0{\cdot}191E + 0{\cdot}545\ V \quad (3)$$

$$\log BB = -0{\cdot}118 \text{ to } 0{\cdot}11A - 1{\cdot}174B - 0{\cdot}176S - 0{\cdot}242E + 1{\cdot}195\ V \quad (4)$$

2.3. Cell culture

U-87 MG glioblastoma cells (ATCC, American Type Culture Collection ATCC®, Old Town Manassas, VA, USA) and normal human fibroblast cells (NHDF) (Lonza, Basel, Switzerland) were cultured in DMEM containing 4.5 g/L glucose, 2 mM L-glutamine with streptomycin and penicillin. Human microvascular endothelial cells HMEC-1 (ATCC) were cultured in MCDB131 medium supplemented with 10 mM L-glutamine, 10 ng/ml FGF (all from ThermoFisher Scientific, Wilmington, DE, USA), 1 μg/ml hydrocortisone (Sigma-Aldrich). THP-1 monocytes from patients with acute leukaemia (ATCC) were cultured in RPMI-1640 (Gibco, Thermo Fisher Scientific) supplemented with 50 μM beta-mercaptoethanol (Sigma-Aldrich). Media were supplemented with FBS

up to 10% (Sigma-Aldrich) and penicillin-streptomycin solution up to 1% of final volume (Sigma-Aldrich). Media were changed twice a week and cells were passaged with TrypLe (Gibco) when confluence did not exceed 70%. Cells were cultured in a humid atmosphere (95%) with 5% CO2 (HeraCell 150i, Thermo Fisher Scientific).

2.4. Monocyte differentiation

THP-1 monocytes were grown as suspension cultures in complete RPMI-1640 medium (Gibco) with the addition of 100 nM PMA (Sigma-Aldrich) [37,38]. After 24 h, monocytes were observed to differentiate into CD68 + macrophages adhering to the bottom of the flask.

2.5. SRB assay

The cytotoxicity of G721–0282 was evaluated in three cell lines using the sulforodhamine B (SRB) assay, which consists of total protein precipitation with TCA (trichloroacetic acid) and spectrophotometric analysis [39], [40]. G721–0282 was diluted in DMSO (Sigma-Aldrich) to a concentration of 100 mM and this stock was further diluted in medium [10]. Cells were seeded onto 96-well plates (TPP, Trasadingen, Switzerland) in 100 µl of medium at the number per well determined during calibration: 2.0×10^3 for U-87 MG (2.2×10^3 cells per 1 cm^2), 3.0×10^3 for HMEC-1 and 6.0×10^3 for NHDF. After 24 h, the medium was changed and 100 µl of concentrations of G721–0282 ranging from 100 to 2.5 µM were added to determine the concentration range for further studies and IC50 (Fig. S1). On this basis, the cytotoxicity of selected concentrations of G721–0282 was determined as a series of dilutions: 100 µM, 50 µM, 25 µM, 12.5 µM and 6.25 µM. A control with medium and a control with DMSO concentrations of 100 µM (0.1%) were included in the experiments. After 24, 48 and 72 h, 50 µl of 50% TCA (4 °C) (Sigma-Aldrich) was added per well and incubated for 1 h at 4 °C. The plates were then gently washed five times with tap water and dried. Next, 50 µl of 0.4% SRB solution in 1% acetic acid was added per well and incubated for 30 min at RT (room temperature). The plates were then gently washed five times with 1% acetic acid, dried and 150 µl of 10 mM TRIS (tris(hydroxymethyl)aminomethane) was added to each well. After 10 min incubation (RT), absorbance was measured at a wavelength of 540 nm using an ELx800 spectrophotometer and Gen5 software (BioTek, Winooski, VT, USA). Cell viability at the concentrations studied, expressed as a percentage of the control, was calculated according to formula (5):

$$[(A_i\text{-}A_m)/(A_c\text{-}A_m)]\times 100 \quad (5)$$

where A_i-Absorbance of investigated concentration, A_m-Absorbance o medium, A_c-Absorbance of control.

2.6. Cell cycle analysis (flow cytometry)

The distribution of cell cycle phases after treatment with G721–0282 was assessed by flow cytometry [41], [42]. U-87 MG cells were seeded onto 6-well plates (TPP) at 2.0×10^4 cells per well (2.2×10^3 cells per 1 cm^2). After 24 h, the medium was discarded and G721–0282 compound was added at concentrations of 100, 50, 25, 12.5 and 6.21 µM and incubated for 72 h. A control with medium and a control with DMSO concentrations of 100 µM were included in the experiment.

The cells were then trypsinised, washed twice in cold (4 °C) phosphate-buffered saline (PBS) and fixed in ice-cold 70% ethanol at 4 °C overnight. The cells were then centrifuged (1050 rpm, 5 min, 4 °C) and rinsed twice in PBS. Samples were stained with a FxCycle™ PI/RNase Staining Solution Kit (Life Technologies, Carlsbad, CA, USA) and incubated for 30 min at 37 °C in the dark. Propidium iodide fluorescence was measured using a BD FACSCanto II flow cytometer on channel 630/22 (Beckton Dickinson, Franklin Lakes, NJ, USA). Data from a minimum of 20,000 events per sample were collected and calculated using ModFit LTTM software, version 4.0.5 (Verity Software House, Inc., Topsham, ME, USA). The experiment was performed in three independent laboratory replicates.

2.7. Apoptosis (flow cytometry)

The flow cytometry method was used to test the intensity of apoptotic induction under the effect of compound G721–0282 [41], [42]. U-87 MG cells were seeded on 6-well plates (TPP) at 2.0×10^4 cells per well. After 24 h, the medium was discarded and G721–0282 compound was added at concentrations of 100, 50, 25, 12.5 and 6.21 µM and incubated for 72 h. A control with medium and a control with DMSO concentrations of 100 µM were included in the experiment.

The cells were then trypsinised, washed twice in PBS and centrifuged (1050 rpm, 5 min). Cells were diluted to 1 × 106 cells/ml and stained with the FITC Annexin V Apoptosis Detection Kit II (Beckton Dickinson, Franklin Lakes, NJ, US) according to the manufacturer's instructions. Data from a minimum of 10,000 events were collected for each sample. The results obtained were further analysed using FlowJo 10.5 software (FlowJo, Asham, OR, USA). The experiment was replicated in three independent laboratories.

2.8. Angiogenesis assay

HMEC-1 cells were used to determine the effect of compound G721–0282 at concentrations of 100, 50, 25, 12.5 and 6.25 µM on tube formation in the presence of CHI3L1 protein (2599-CH, R&D Systems, Minneapolis, MN, USA) at two concentrations: 0.6 µg/ml and 2.4 µg/ml. In addition, G721–0282 alone was used to determine the influence of this compound independently of CHI3L1 protein, and a control was included with medium and medium containing DMSO at a concentration equivalent to 100 µM of the inhibitor under investigation. The same scheme was used for U-87 MG cells to determine the tube-like structure in vascular mimicry formation.

Cells were harvested thoroughly with TrypLE (Gibco, ThermoFisher), washed in PBS and suspended in DMEM medium (Lonza) without FBS and with appropriate concentration of G721–0282. Recombinant human CHI3L1 protein (R&D) was then added to give a protein concentration of 0.6 µg/ml and 2.4 µg/ml, respectively. For all angiogenesis experiments, 2.0×10^4 cells per well were suspended in 100 µl in a 96-well plate (TPP) and loaded onto the top of Geltrex (ThermoFisher) [43], [44]. After 24 h, tube structures were analysed using an inverted phase contrast microscope CKX53 (Olympus, Tokyo, Japan) and counted in five random fields from each well. The amounts of tube structures were expressed as a percentage of the control. Experiments were performed in triplicate.

2.9. Scratch assay

U-87 MG cells were seeded onto coverslips in 6-well plates (TPP) at 5.3×10^4 cells per well ($2.3 \times 10^3/cm^2$). After 24 h, the cells were scratched with 1000 µl tips [45,46], the medium was discarded and replaced with G721–0282 at concentrations of 100, 50, 25, 12.5 and 6.25 µM. A control with medium and a control with DMSO at a concentration equal to 100 µM of the inhibitor of interest were included in the experiment. The cells were cultured for 72 h, then the medium was changed and the addition of G721–028 and controls was repeated for the next 72 h. The cells were then washed twice in cold PBS (Lonza), fixed in ice-cold methanol for 10 min (Chempur®, Piekary Slaskie, Poland) and treated with 0.5% crystal violet in 25% methanol solution for 10 min (Sigma-Aldrich®) [47]. Microscopic evaluation was performed using a BX41 light microscope (Olympus).

2.10. Behaviour of U-87 MG cells in culture with G721-0282

U-87 MG cells were seeded on T-25 flasks (Thermo Fisher) at 5.7 ×

10^4 cells (2.3 $\times 10^3/cm^2$). After 24 h, the medium was discarded and fresh medium containing G721–0282 at concentrations of 100, 50, 25, 12.5 and 6.25 μM was added. A control culture with medium and control containing DMSO at a concentration equivalent to 100 μM of the inhibitor of interest was included in the experiment. Cells were cultured for 72 h, then the medium was changed and the addition of G721–028 and controls was repeated for the next 72 h.

2.11. Cytoskeletal architecture

U-87 MG cells were seeded on glass slides at $3 \times 10^3/cm^2$ in medium containing G721–0282 at concentrations of 100, 50, 25, 25, 12.5 and 6.26 μM, and medium control and solvent control (0.1% DMSO) were also included in the experiment. After 72 h, the media were changed and replaced with fresh media in the same scheme and incubated for the next 72 h. The influence of G721–0282 on cytoskeletal rearrangements in U-87 MG cells via β-actin, β-tubulin and F-actin was then visualised by immunofluorescence reaction [42], [48].

2.12. Multiplex analysis

The human cytokine and chemokine growth factor assay of the Milliplex map kit (HCYTA-60 K, Millipore, Merck, Darmstadt, Germany) [49], [50] was performed in the cell lysate and corresponding supernatants from two-week spheroids treated with G721–0282 compound concentrations (100, 50, 25, 25, 12.5 and 6.26 μM). Spheroid lysates were prepared in neutral buffer containing cold PBS. A Pro250 homogeniser (PRO Scientific Inc., Oxford, CT, USA) was used. After homogenisation, they were centrifuged at 15,000 x g for 10 min. The supernatant was collected and used for the assay. The assay was performed according to the manufacturer's instructions. First, the test plate was washed with wash buffer, shaken for 10 min and decanted. The standard (prepared immediately before use), control, test lysates and supernatants were then added to the wells. Assay buffer and antibody-immobilised beads were then added in equal volumes. The test plate was incubated for 2 h at room temperature with shaking. The removed well contents were then washed three times with wash buffer and detection antibodies were added for 1 h at room temperature. Streptavidin-phycoerythrin was then added for 30 min at RT. The contents of the wells were then removed and washed three times with wash buffer. Finally, sheath fluid was added and read using Luminex (Riverside, CA, USA).

2.13. Spheroids formation

U-87 MG and HMEC-1 cells and macrophages were counted, mixed 1:1:1, centrifuged (300 g for 10 min) and seeded onto low-adhesion cell culture flasks (Equimed, Wroclaw, Poland) or 24-well plates (Equimed). Spheroids were formed after 24 h. Spheroids were cultured in complete DMEM medium for two periods: one month and two weeks. The culture medium was changed three times per week. Types containing NHDF cells were also prepared to optimise spheroid formation.

2.14. Development of 3D spheroids with G721-0282

U-87 MG and HMEC-1 cells were seeded together with macrophages on a low adhesion 96-well plate (3D PrimeSurface® 96 V, MS-9096VZ, Akita Sunitomo Bakelite, Akita, Japan) [51], [52] at 2×10^3 of each cell in 100 μl of G721–0282 compound concentrations: 100, 50, 25, 12.5 6.21 μM and control without compound. After 72 h, the media and media with G721–0282 concentrations were replaced with fresh media in the same scheme. The culture was maintained in complete DMEM medium for fourteen days with media changes twice a week. At the end of the experiments, the spheroids were embedded in paraffin and the control was fixed for TEM analysis.

2.15. Spheroids treatment with G721-0282

Spheroids were treated with G721–0282 compound concentrations (100, 50, 25, 25, 12.5 and 6.26 μM) in 24-well plates for 72 h. After 72 h, the media and concentrations of the tested compound were replaced with fresh media for a further 72 h. After this time, a portion of the 1 month cultured spheroids were fixed for transmission electron microscopy (TEM), immunohistochemistry (IHC) and immunofluorescence (IF) reactions, and also stored at − 80 °C for Western blot and ddPCR analysis. Spheroids cultured for two weeks were fixed or harvested for IHC, IF and multiplex chemokine/cytokine assays. The supernatant was also collected.

2.16. Paraffin-embedded 3D spheroids

At the end of the experiments, spheroids were counterstained in haematoxylin (4 min) and fixed in cold 4% PFA (paraformaldehyde) (4 °C, overnight). The next day, spheroids were embedded in 2% agarose and then in paraffin blocks (according to [53] with own modifications). Slides for immunohistochemical and immunofluorescence analysis were prepared in a typical manner for tissue slides.

2.17. Immunohistochemistry

Immunohistochemistry was performed on 4 μm sections of spheroids and tissue samples. Deparaffinisation and antigen retrieval were performed in PT-Link (Dako, Glostrup, Denmark) using EnVision FLEX Target Retrieval Solution (97 °C, 20 min; pH 6.0 for CD31 and GFAP and pH 9.0 for CHI3L1, CD68, IBA1) [10,11,54,55]. Blocking was performed in 1% BSA (bovine serum albumine) (RT, 30 min), followed by endogenous peroxidase blocking with EnVision FLEX Peroxidase Blocking Reagent (Dako) (RT, 5 min). Slides were collected and incubated overnight at 4 °C with anti-CD31 antibody specific for endothelial cells (1:500, mouse monoclonal, ab9498, Abcam, Cambridge, UK), anti-GFAP (glial fibrillary acid protein) antibody specific for neuronal cells (1:500, mouse monoclonal, ab27929, Abcam), pan-macrophage anti-CD68 antibody (1: 100, mouse monoclonal, MSK055–05, Zytomed, Berlin, Germany), specific for microglia and macrophages, anti-IBA1 antibody (1:500, rabbit polyclonal, 019–19741, FUJIFILM Wako, Osaka, Japan), macrophage M2 phenotype anti-CD163 antibody (1: 500, rabbit polyclonal, sc-33560, Santa Cruz, Dallas, TX, USA), cancer stem cell anti-CD133 antibody (1:250, mouse monoclonal, MAB11331, R&D) and anti-CHI3L1 (1:50, goat polyclonal, AF2599, R&D). Incubation with secondary antibodies was performed using EnVision FLEX/HRP (RTU, Dako, 1 h, RT) for mouse and rabbit antibodies and in donkey anti-goat secondary antibodies conjugated to HRP (1:400, Jackson ImmunoResearch, Suffolk, UK). All antibody dilutions were prepared in 1% BSA in PBS/0.1% Tween20. Slides were then incubated with EnVision Flex substrate buffer (Dako) containing DAB (10 min, RT) and counterstained with EnVision Flex Hematoxilin Solution (Dako) (5 min, RT). Slides were coverslipped with Dako Mounting Medium (Dako).

2.18. Immunofluorescence

Immunofluorescence was performed on 4 μM spheroid slides and deparaffinisation and antigen retrieval were performed as described for immunohistochemistry. For immunofluorescence reactions performed on U-87 MG cells and macrophages cultured on coverslips, these steps were omitted in favour of 4% PFA fixation (10 min, RT) and 0.2%. TritonX-100 permeabilization (12 min, RT) [42], [48]. All slides were blocked in 1% BSA in PBS/0.1% Tween20 (0.5 h, RT) and primary antibodies were used: CD31 (1:500, mouse monoclonal ab9498, Abcam), anti-GFAP (1:500, mouse monoclonal ab27929, Abcam), anti-CHI3L1 (1:50, goat polyclonal AF2599, R&D), anti-CD163 (1: 500, rabbit polyclonal, sc-33560, Santa Cruz), β-actin antibody (1:500, mouse monoclonal (Ba3R) MA5–1739, Invitrogen, Thermo Fischer) and

β-tubulin antibody (1:500, rabbit monoclonal, ab6046, Abcam). All primary antibodies were diluted in 1% BSA in PBS/0.1% Tween20 and slides were incubated overnight at 4 °C. Fluorochrome-conjugated secondary antibodies (dilution 1:2000, incubation 1 h RT) were then applied: goat anti-mouse Alexa 488 (ab150113, Abcam), goat anti-rabbit Alexa594 (ab150080, Abcam), goat anti-rabbit Alexa568 (ab175470, Abcam) and donkey anti-goat Alexa647 (ab150131, Abcam). All antibodies were diluted in 1% BSA in PBS/0.1% Tween20. Phalloidin STAR RED (1:200, Abberior GmbH, Göttingen, Germany), used to detect F-actin filaments, was applied after blocking for 1 h RT. Fluoroshield mounting medium with DAPI (ab104139, Abcam) was used to cover the slides. Immunofluorescence visualisation was performed using a confocal microscope (Fluoview FV3000, Olympus) and Cell Sense imaging software (Olympus).

2.19. Transmission electron microscopy (TEM)

Spheroids were chemically fixed at RT in a 3.6% (v/v) glutaraldehyde solution (SERVA Electrophoresis, Heidelberg, Germany) prepared in 0.2 M cacodylate buffer (pH 7.2–7.4) with saccharose (Chempur) [42], [47]. After 25 min, the fixative was rinsed three times with cacodylate buffer (0.1 M). The spheroids were then enclosed in the fibrin clot after droplets of bovine thrombin (Biomed, Lublin, Poland) and fibrinogen (3 mg/ml; Merck KGaA, Darmstadt, Germany), both dissolved in PBS, were added to the falcon tubes. The cells were then exposed to fixation in 1% (w/v) osmium tetroxide OsO4 (SERVA Electrophoresis) prepared in 0.1 M cacodylate buffer (1 h, RT). The OsO4 was then rinsed with cacodylate buffer and the samples were progressively dehydrated in increasing concentrations of ethanol (30–90%) and a mixture of 90% ethanol/90% acetone and finally passed through a graded acetone series (90%, 95% and 100%; Stanlab, Lublin, Poland). Prior to the embedding process, the samples were immersed overnight in the mixture of acetone and epoxy resin (Epon 812, SERVA Electrophoresis) at a ratio of 3:1 (20 min), 1:1 (60 min) and 1:3 (60 min). The infiltration process was carried out in an oven at 60 °C in flat embedding moulds (Pelco, Ted Pella, Redding, CA, USA) filled with an epoxy resin containing 2,4,6-tris(dimethylaminomethyl)phenol to accelerate the curing of the resin. After several days, the epoxy resin was removed until only the spheroids were exposed and then cut into semi-thin sections (600 nm thickness) using a histo-diamond knife (Diatome, Nidau, Switzerland) and stained with toluidine blue (Serva Electrophoresis) and anhydrous sodium carbonate (Alchem, Toruń, Poland). The epoxy blocks were then mounted on the Power Tome XL ultramicrotome (RMC, Tucson, AZ, USA) and serial ultrathin sections of 70 nm thickness were cut using an ultra 45° diamond knife (Diatome). The ultrathin sections were carefully mounted on 200 mesh rhodium-copper grids (Maxta form, Ted Pella, Redding, CA, USA) to avoid overlap. The grids were placed in a Petri dish for 24 h and then counterstained with the UranyLess solution and Reynold's lead citrate 3%, (Electron Microscopy Sciences, Hatfield, PA, USA) on top of the drops for 2 min. The grids were then rinsed by vertical movements in beakers in 5 changes of demineralised water and allowed to dry for 30 min before observation under a JEM-1011 transmission electron microscope (JEOL, Tokyo, Japan) at 80 kV accelerating voltage. The spheroids were documented at magnifications ranging from 3 to 200 K using a TEM imaging platform iTEM1233 (Olympus, Münster, Germany) connected to a Morada camera.

2.20. Human tissue samples

Glioblastoma, astrocytoma and hemangioblastoma specimens were obtained from patients diagnosed and operated at the Department and Clinic of Neurosurgery, Poznan Medical University, Poland, and stored at − 80 °C. Approval to conduct this research was obtained from the Bioethics Committee of the Medical University of Wroclaw (No. KB-2017/2022).

2.21. The Droplet Digital PCR™ (ddPCR)

Droplet digital PCR was used to determine the absolute number of gene mRNA copies in the analysed materials. Total RNA was isolated using the RNeasy Mini Kit (Qiagen, Hilden, Germany). Reverse transcription (RT-PCR) was performed using iScript™ Reverse Transcription Supermix for RT-qPCR (Bio-rad, Hercules, CA, USA) according to the manufacturer's protocol. An input of 35 ng RNA from each sample was reverse transcribed using a C1000 Touch thermal cycler (Bio-Rad). Reaction conditions were as follows: priming for 5 min at 25 °C, reverse transcription for 20 min at 46 °C and final inactivation of reverse transcriptase for 1 min at 95 °C. The ddPCR reaction mixtures contained 2.5 μl RT product, 1 μl TaqMan-specific probe (Applied Biosystems, Foster City, CA, USA), 7.67 μl molecular biology grade water and 10 μl 2X ddPCR™ MasterMix for Probes (Bio-Rad). The TaqMan specific probes used in the experiment to assess the mRNA expression of the genes under investigation were Hs01072228_m1 (CHI3L1), Hs00900055_m1 (VEGFA), Hs01099203_m1 (VEGFC), Hs01128659_m1 (FIGF/VEGFD). The 20 μl reaction mixtures were loaded into a plastic cartridge (Bio-Rad) with 50 μl Droplet Generation Oil for Probes (Bio-Rad) in the QX100 Droplet Generator (Bio-Rad). Droplets from each sample were then transferred to a 96-well PCR plate (Eppendorf, Hamburg, Germany). PCR amplification was performed in a C1000 Touch Thermal Cycler (Bio-Rad) under the following conditions: enzyme activation for 10 min at 95 °C, followed by 40 cycles of denaturation (30 s, 94 °C) and annealing/extension (1 min, 60 °C) and a final enzyme deactivation for 10 min at 98 °C and 10 min at room temperature (RT). Finally, the plate was loaded onto a Droplet Reader (Bio-Rad) and read automatically. The absolute quantification of each mRNA was calculated from the number of positive counts per panel by using the Poisson distribution. The quantification of the target mRNA is expressed as the number of copies/μl (AQ) in the PCR reaction mixture [53], [56].

2.22. Western blot

Cell samples were lysed with RIPA buffer containing EDTA, protease inhibitor cocktail (Heat™ Protease Inhibitor Coctail ×100) and 0.5 mM PMSF (phenylmethanesulfonyl fluoride) (all from Thermo Scientific) [10,53]. An additional syringe was used for spheroid lysis to improve disruption. Tissue samples were homogenised using a TissueRuptor homogeniser (Qiagen, Hilden, Germany) in T-PER tissue protein extraction reagent containing EDTA, protease inhibitors and PMSF. Total protein levels were determined using bicinchoninic acid (Pierce BCA Protein Assay Kit) and the NanoDrop1000 (Thermo Fisher). Lysates were denatured in sample buffer (250 mM TRIS pH 6.8, 40% glycerol, 20% (v/v) β-mercaptoethanol, 0.33 mg/ml bromophenol blue, 8% sodium dodecyl sulphate (SDS)) for 5 min at 95 °C. SDS-PAGE separation was performed on 10% or 12% polyacrylamide gel in a Mini Protean 3 apparatus (Bio-Rad) at 30 μg protein per lane according to the Laemmli method [57]. Tris-glycine buffer for protein transfer contains 20% methanol and 0.05% SDS. PVDF 0.45 μm (polyvinylidene difluoride) (Immobilon®, Millipore, Bedford, MA, USA) membranes were used for transfer 1 h at 140 V (for most protein separations) and nitrocellulose 0.20 μm membranes (Bio-Rad) for transfer 0.5 h at 70 V were used for VEGF-A and VEGF-C proteins. The membranes were blocked in 5% milk in 0.05% TBST, except for CHI3L1, which was blocked in 5% BSA/0.05% TBST and incubated overnight at 4 °C with primary antibodies against CHI3L1 (1:1000, goat polyclonal, AF2599, R&D), β-tubulin (1:1000, in 0. 1% BSA in 0.1% TBST, rabbit polyclonal, ab6046, Abcam), GAPDH (1:1000, in 5% milk in TBST 0.05%, rabbit monoclonal, 2118, Cell Signalling, Denver, MA, USA), VEGF-A (1:1000, in 5% milk in TBST 0. 05%, mouse monoclonal, M7273, Dako, Glostrup, Denmark), VEGF-C (1:1000, mouse monoclonal, 101-M90, ReliaTech, Wolfenbüttel, Germany), VEGF-D (1:1000, in 5% milk in TBST 0. 05%, mouse monoclonal, MAB286, R&D), STAT-3 (1:1000, in 0.1% TBST, rabbit polyclonal, A11185, ABclonal, Woburn, MA, USA), p-STAT-3

(1:1000, in 5% milk in 0.05% TBST, rabbit monoclonal, ab76315, Abcam). The membranes were then washed three times in 0.05% TBST or TBSTX0.2% for CHI3L1 and incubated for 1 h RT with horseradish peroxidase (HRP)-conjugated secondary antibodies using donkey anti-rabbit antibody (1:6000) or donkey anti-mouse antibody (1:3000) (both in 5% milk in 0. 0.05% TBST, Jackson ImmunoResearch, Suffolk, UK) or donkey anti-goat (1:10000 in TBST, Jackson ImmunoResearch). Chemiluminescence was performed using Luminata Classico Immobilon Western HRP Substrate, Luminata Forte Immobilon Western HRP Substrate or SuperSignal West Femto Chemiluminescent Substrate (Thermo Fisher). ImageLab software (Bio-Rad) and ChemiDocTM MP system (Bio-Rad) were used for visualisation with exposure times ranging from 1 s to 3 min

2.23. Label-free digital holographic tomography (DHT)

DHT is based on quantitative phase imaging and allows reconstruction of the RI, which is used as an image contrast for 3D visualisation of living cells. Furthermore, DHT provides label-free 3D morphological and optical information with submicron or even subnanometre resolution beyond the optical diffraction limits characteristic of conventional microscopy techniques, including scanning confocal fluorescence microscopy [58,59], is non-destructive or does not require time-consuming and costly sample preparation procedures as in TEM microscopy.

Cells were seeded at 3.4×10^3 (2.2×10^3 cells per 1 cm^2) cells per dish (Ibidi, Gräfelfing, Germany) in 600 µl of complete DMEM medium containing the following concentrations of G721–0282 compounds: 100 µM, 50 µM, 25 µM, 12.5 µM, 6.25 µM. The experiment included a control with culture medium and a control with solvent (0.1% DMSO). After 72 h, the media and concentrations of the tested compound were replaced with fresh ones and the incubation continued for another 72 h. DHT methods were then used to assess the influence of the inhibitor concentration on live glioblastoma cells.

DHT was used to qualitatively and quantitatively investigate the effect of different inhibitor concentrations on glioblastoma cells. A schematic of the measurement procedure and data analysis is shown in Fig. 6A. A digital holotomograph (3D Cell Explorer, Nanolive, Tolochenaz, Switzerland) with a dry microscope objective (60 ×, numerical aperture NA=0.8, Nikon) was used to visualise the spatial distribution of the refractive index (RI) in the form of 3D-RI tomograms of the investigated glioblastoma cells. Each 3D-RI tomogram was numerically reconstructed from a series of digital holograms (DH) acquired at different illumination angles. The numerical reconstruction of the 3D-RI tomograms was performed using the STEVE software (version 1.6.3496, Nanolive, Tolochenaz, Switzerland).

Based on the reconstructed 3D-RI tomograms, the cells and characteristic intracellular structures could be digitally stained based on their RI values to obtain the rendered 3D visualisation of the cells. The glioblastoma cell samples studied were divided into seven groups: reference cells incubated in nutrient medium (C), cells incubated with nutrient medium and inhibitor solvent (SC), and cells incubated with five different concentrations of the inhibitor G721–0282: 100 µM, 50 µM, 25 µM, 12.5 µM, 6.25 µM. For each group, at least 15 3D RI tomograms were reconstructed from the 96 2D RI tomograms of the cells. The thresholding of the RI histogram was used to distinguish the regions of individual cells and to perform segmentation based on the dedicated algorithm developed in MATLAB® software (version R2021b, MathWorks, Natick, MA, USA). Based on the 2D-RI tomograms representing the central cross-section through the cells, digital staining based on the RI values of specific intracellular structures such as cytoplasm, nucleus, nucleoli and lipid droplets was performed to obtain the 3D visualisations of the studied cells.

The inhibitor-induced changes in RI values within the cells caused by the different concentrations of inhibitor were investigated quantitatively. First, the variation of the average 3D RI values of whole cells from each group was analysed. Then, to investigate the influence of the inhibitor concentration on the cellular structures, their average RI values were extracted from segmented 3D-RI tomograms and analysed. The inhibitor used affects the protein concentrations inside the cells, so the RI values of the cells and their structures should differ from the control samples. As the RI value of cell structures is directly related to cell dry mass or dry mass density, which is an important biophysical parameter, it can also provide additional information to characterise inhibitor-induced changes in the chemical composition of the cells. Particular attention has been paid to changes in the intracellular protein concentration of cellular structures. RI data provide information on the local concentration of non-aqueous molecules such as proteins, sugars, lipids and nucleic acids within cells. The RI is linearly proportional to the chemical concentration of these molecules [60]. Therefore, based on RI data, dry mass density can be derived from RI using a linear calibration model (formula 6) [61], [62]:

$$drymassdensity = \frac{1}{\alpha}\left(\frac{RI_S}{RI_{medium}} - 1\right)\left[\frac{g}{dL}\right] \quad (6)$$

where α is the proportionality constant called the RI increment, RIs is the mean value of the RI of the examined cellular structure, and RI_{medium} is the mean value of the medium surrounding the cells. RI increment values vary in the range of 0.18–0.21 ml/g [47]. Since the inhibitor should only affect the concentration of proteins, the α of 0.185 ml/g, known to be a typical value for proteins [18], [19], was used to determine the dry mass density of the cytoplasm. In the case of the nucleus, the evaluated α was the average of its typical value for nucleic acids (0.170 ml/g) and proteins (0.185 ml/g). Furthermore, taking into account the fact that lipid droplets usually contain not only lipids but also proteins attached to their surface, the RI increment of 0.160 ml/g was used as the average of its typical value for proteins (0.185 ml/g) and lipids (0.135 ml/g).

2.24. Statistical analysis

Normality of distribution was analysed using the Shapiro-Wilk test. Statistical analysis was performed using one-way ANOVA with Tukey's post-hoc tests for multiple comparisons. Statistical significance was defined as $p < 0.05$. The existence of statistically significant differences between the RI values of individual cells and their structures was confirmed by one-way ANOVA. If the determined p-value (Prob>F) for the F-statistic is less than the assumed significance level (in our case 0.05), the test rejects the null hypothesis that all group means are equal. The normality assumption of the extracted average 3D-RI values was tested using the Anderson-Darling test. Prism 9.4.1 (GraphPad, La Jolla, CA, USA) was used for statistical analysis.

3. Results

3.1. Theoretical calculations of BBB permeation of G721-0282 compound

The calculated values of the logBB for the studied compound were found to be: 0.29 (Eq.1), 0.47 (Eq.2), 0.03 (Eq.3) and 0.12 (Eq.4). It is generally accepted that drugs with logBB> 0.3 readily cross the blood-brain barrier readily, whereas molecules with logBB< −1 are poorly distributed in the brain [63], [64]. The predicted logBB for G721–0282 suggests an ability to cross the blood-brain barrier. We also calculated the probability of crossing the blood-brain barrier by a procedure using machine learning and resampling methods [65]. The probability was calculated using the web tool admetSAR. The obtained probability is 0.9795.

3.2. SRB

Cytotoxicity evaluation showed that G721–0282 decreased the

viability of U-87 MG glioblastoma cells most significantly at 72 h, but didn't reach the IC50 level. In normal fibroblast cells NHDF and endothelial cells HMEC-1, viability was mostly decreased after 24 and 48 h of incubation, but after 72 h G721–0282 didn't cause any cytotoxicity effect (Fig. 1D), even at a wide range of concentrations (Fig. S1).

3.3. Cell cycle

Cell cycle analysis differentiated U-87 MG cells into two subpopulations of diploid and aneuploid cells. The analysis showed that G721–0282 didn't induce G1 phase in the diploid subpopulation, but rather decreased it at 25 μM. However, at 100 μM we observed a significant decrease in G1 phase in aneuploid cells. At 25 μM of G721–0282 a decrease in S phase was clearly visible. In diploids, the lowest percentage of cells in S phase was observed at 100 μM (Fig. 1A).

In the diploid subpopulation, the percentage of cells in G2 phase was significantly higher after treatment with 100 μM G721–0282. Arrest in the G2 phase of the cell cycle was also observed in aneuploids at 100 μM (Fig. 1A).

3.4. Apoptosis

The percentage of apoptotic cells in U-87 MG cells was high at 12.5 μM and 6.25 μM, but was highest after incubation with 100 μM G721–0282 (Fig. 1B).

3.5. Necrosis

The percentage of U-87 MG cells with ongoing necrosis was significantly higher after treatment with 100 μM compared to other groups (Fig. 1C).

3.6. Angiogenesis

In an experiment with the addition of 0.6 μg/ml recombinant CHI3L1 protein, the formation of tube-like structures in HMEC-1 cells was reduced at a concentration of 100 μM G721–0282 and at 100 μM and 50 μM with the addition of 2.4 μg CHI3L1. HMEC-1 cells formed the most tubes at 2.4 μg/ml CHI3L1 protein. No statistical differences in the number of tubes were observed in HMEC-1 cells treated with G721–0282 alone, without CHI3L1 (Fig. 2A). Endothelial cell density was also reduced in spheroids developed in the presence of G721–0282 and cultured for 2 weeks (Fig. 2B).

In U-87 MG cells, G721–0282 inhibited the formation of tub-like structures in the presence of 0.6 μg/ml CHI3L1. In the presence of 2.4 μg/ml CHI3L1, the most effective inhibition of tube-like structure formation occurred at 100 μM G721–0282. When G721–0282 was added alone, 100 μM and 50 μM concentrations inhibited tube formation (Fig. 3).

3.7. Scratch assay

After incubation of U-87 MG cells with G721–0282, no differences were observed after 72 h, but prolonged incubation with the inhibitor for the next 72 h showed a decrease in cell migration at the highest concentration (100 μM) (Fig. 4A). Decreased cell motility was also observed in standard U-87 MG cells cultured with CHI3L1 inhibitor (Fig. 4B and C).

3.8. Cytoskeletal architecture

Immunofluorescence reactions showed a lower density of β-tubulin filaments in U-87 MG cells after prolonged treatment (2 ×72 h) with two highest concentrations of G721–0282: 100 μM and 50 μM, compared to controls. A similar result was observed for F-actin filaments stained with phalloidin, where phillopodia formation was reduced at 100 μM, 50 μM and 25 μM (Fig. 4C and D).

3.9. Immunohistochemical reactions (IHC)

IHC reactions showed the presence of CD31-positive endothelial cells in spheroids, CD163-positive M2 macrophages and also the presence of cells of neuronal origin expressing GFAP and CHI3L1. IBA1 expression was also detected in microglial cells and macrophages (Fig. 4E). Expression of CD68, a pan-macrophage marker, is typical for U-87 MG cells [66] (data not shown). In addition, CD133-positive cancer stem cells were observed in the spheroids. For comparison, expression of these markers was also observed in glioblastoma tissue (Fig. 4E). Interestingly, CD31 expression was also observed in spheroids initially growing in G721–0282, and we observed a decreased density of CD31-positive cells at 100 μM G721–0282 (Fig. 4E).

3.10. Immunofluorescence reactions

The results of the immunofluorescence reactions performed allowed the detection of CD31 + endothelial cells coexisting with glioma U-87 MG cells expressing CHI3L1 and GFAP, as well as CD163 + macrophages (Fig. 4D).

3.11. TEM

Two types of spheroids were created in the in vitro experiments to assess the morphology and relationships of the different cells in the tumour microenvironment. The TEM method was used after increasing the contrast of the cell membranes with lead citrate and UranyLess contrast to assess the morphological characteristics of the cells inside the spheroids. Four distinct cell types were identified. Fibroblasts (Fig. S2) were elongated and contained a euchromatic, elongated nucleus with islands of heterochromatin and one or two large nucleoli with a distinct granular component, fibrillar centre and dense fibrillar component. In the cytoplasm, interconnected dilated tubules and sacs of rough endoplasmic reticulum, prominent and well-developed cisternae of dictyosomes, lipid droplets, round or rod-shaped mitochondria with lamellar cristae and abundant cytoskeletal components were detected. Fibroblasts were surrounded by extracellular matrix components such as ground substance and fibres. Characteristic features of macrophages were numerous lipid droplets and lysosomes, a single nucleus but with multiple nuclear envelope invaginations; electron dense cytoplasm containing many rod-shaped mitochondria. The most striking feature was the long cytoplasmic processes extending from the cell membrane towards the dead cells. Large and electron-bright glial cells have polylobate euchromatic nuclei with some heterochromatin clumps, numerous lipid droplets, cisternae of the Golgi apparatus and many rod-shaped mitochondria with lamellar cristae and autophagic vacuoles with various contents surrounded by multiple membranes. In addition, the rough endoplasmic reticulum formed concentric circles.

The endothelial cells were spherical with round nuclei, a single nucleolus, many encapsulated vesicles and vacuoles in the cytoplasm. In addition, the cells in the spheroids cooperate by developing intercellular junctions of two different patterns (cell-to-cell adherent or tight) or the tips of the cytoplasmic processes of the same cells adhere to each other. The cells also produce cytoplasmic processes that engulf the other cells (Fig. 4F).

3.12. Multiplex analysis

A decreasing effect of G721–0282 on IL-1β expression levels in spheroids was observed, with the lowest levels at 100, 25 and 6.25 μM. The highest levels of IL-1β were observed at 50 and 12.5 μM, but increased in the solvent control compared to the medium control. The level of IL-1β in the supernatants was inversely proportional to the concentration of G721–0282, although a trend towards increased levels

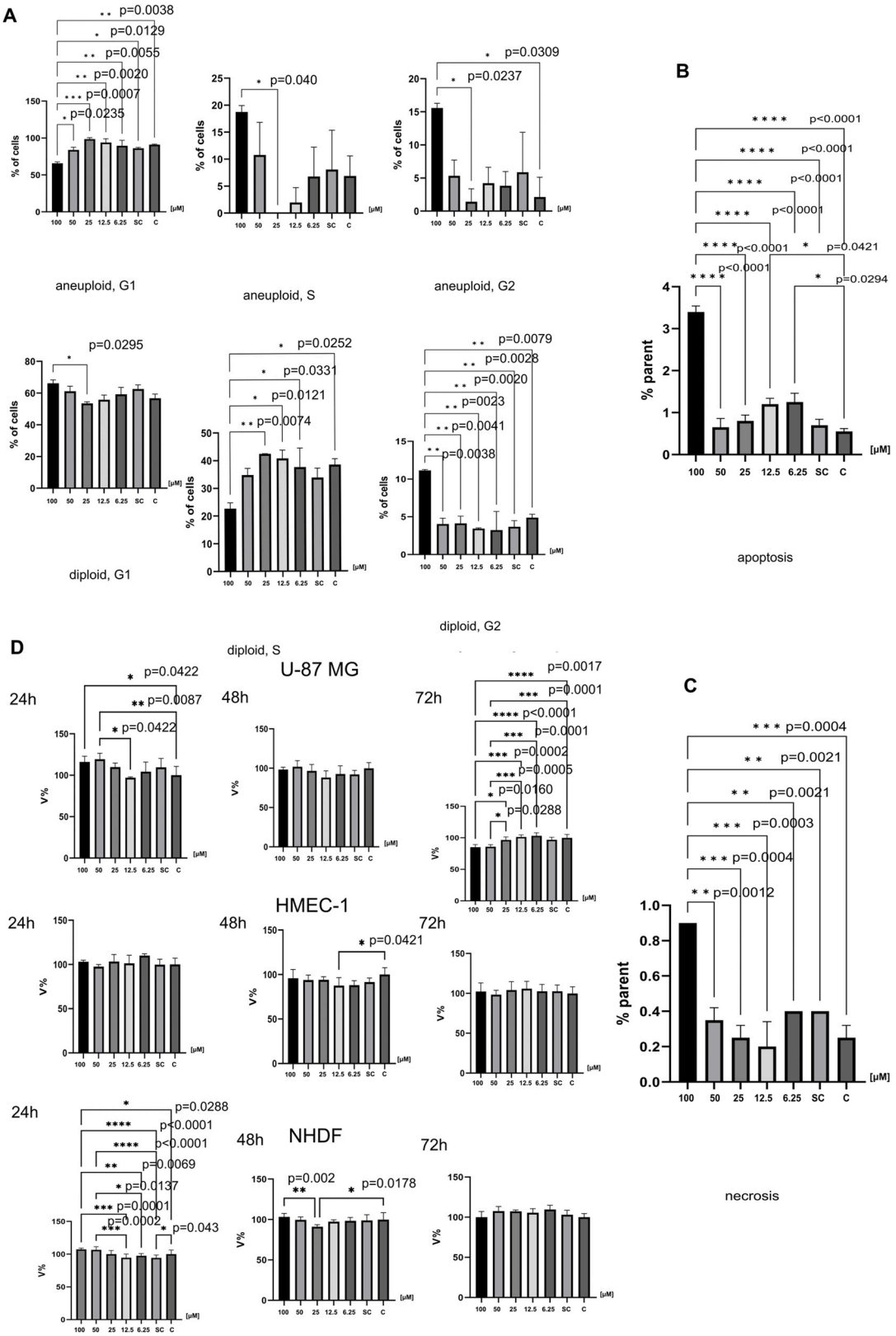

Fig. 1. Cell cycle analysis and cytotoxicity in G721–0282 treatment. Influence of G721–0282 on U-87 MG cell cycle -**A** in aneuploid and diploid subpopulation and on induction of apoptosis -**B** and necrosis -**C** at five concentrations. Analysis of changes in cell viability -**D** after G721–0282 treatment was performed on human U-87 MG glioblastoma cells, microvascular endothelial cells HMEC-1 and dermal fibroblasts NHDF using the SRB assay. A control (C) with medium and a control with DMSO concentrations of 100 μM of G721–0282 (SC solvent control) were included in the experiments. One-way ANOVA Tukey's post-hoc tests were performed for multiple comparisons.

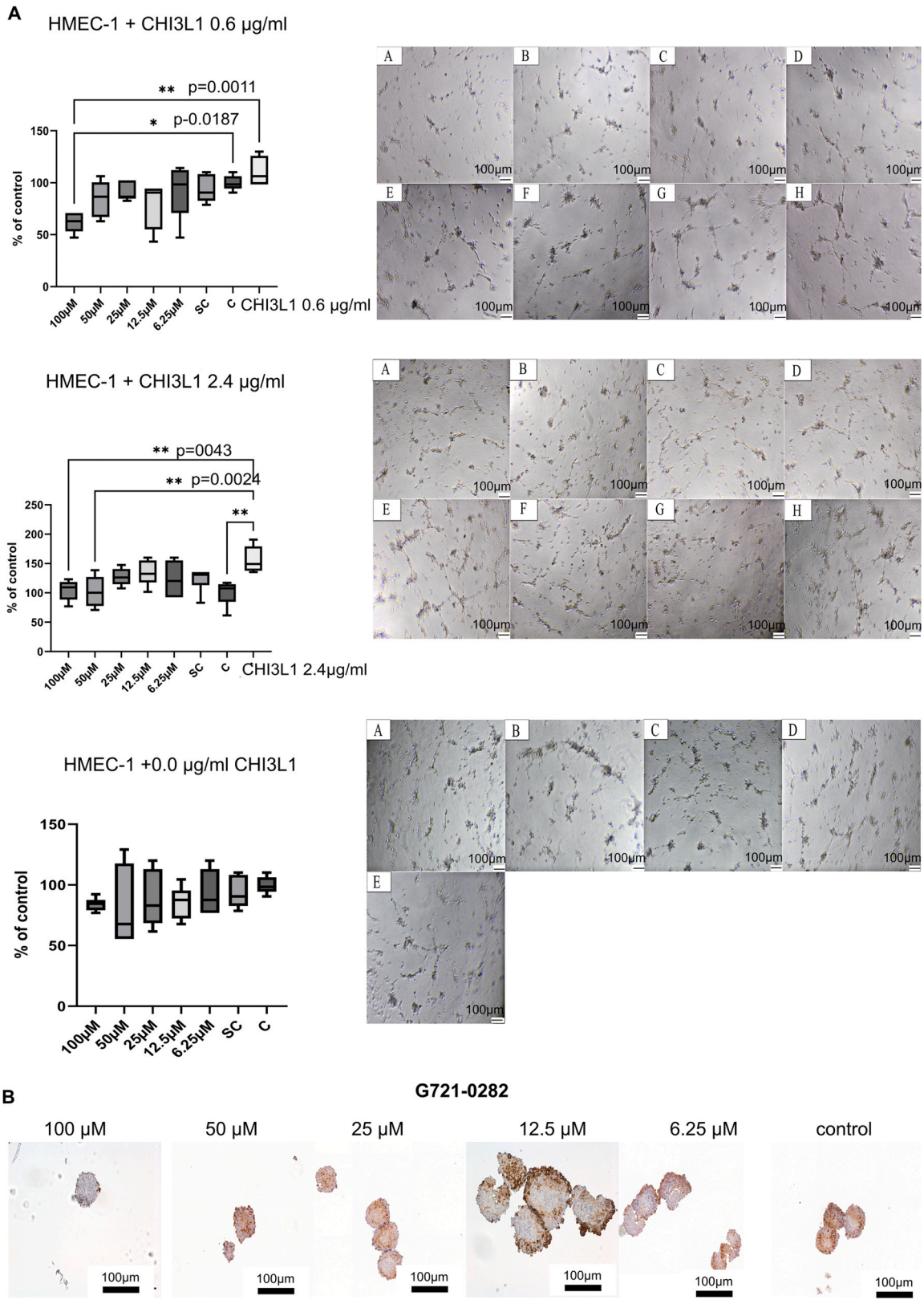

Fig. 2. Inhibition of CHI3L1-dependent angiogenesis in in vitro models. Angiogenesis inhibition by G721–0282 in tube formation assay with microvascular endothelial cells HMEC-1 -**A** in the presence of recombinant CHI3L1 protein and CHI3L1 inhibitor: G721–0282 at five concentrations: 100 µM (A), 50 µM (B), 25 µM (C), 12.5 µM (D), 6.25 µM (E), (F) solvent control (SC; control containing DMSO concentrations found in 100 µM of G721–0282) and control (G). Control with addition of G721–0282 without CHI3L1 was included in the experiments. One-way ANOVA with Tukey's post-hoc test was performed. Effectiveness of angiogenesis inhibition was also investigated on spheroid model -**B** consisting of U-87 MG cells, HMEC-1 cells and macrophages and growing in presence of CHI3L1 inhibitor. Immunohistochemical reactions were performed to localise CD31 + endothelial cells.

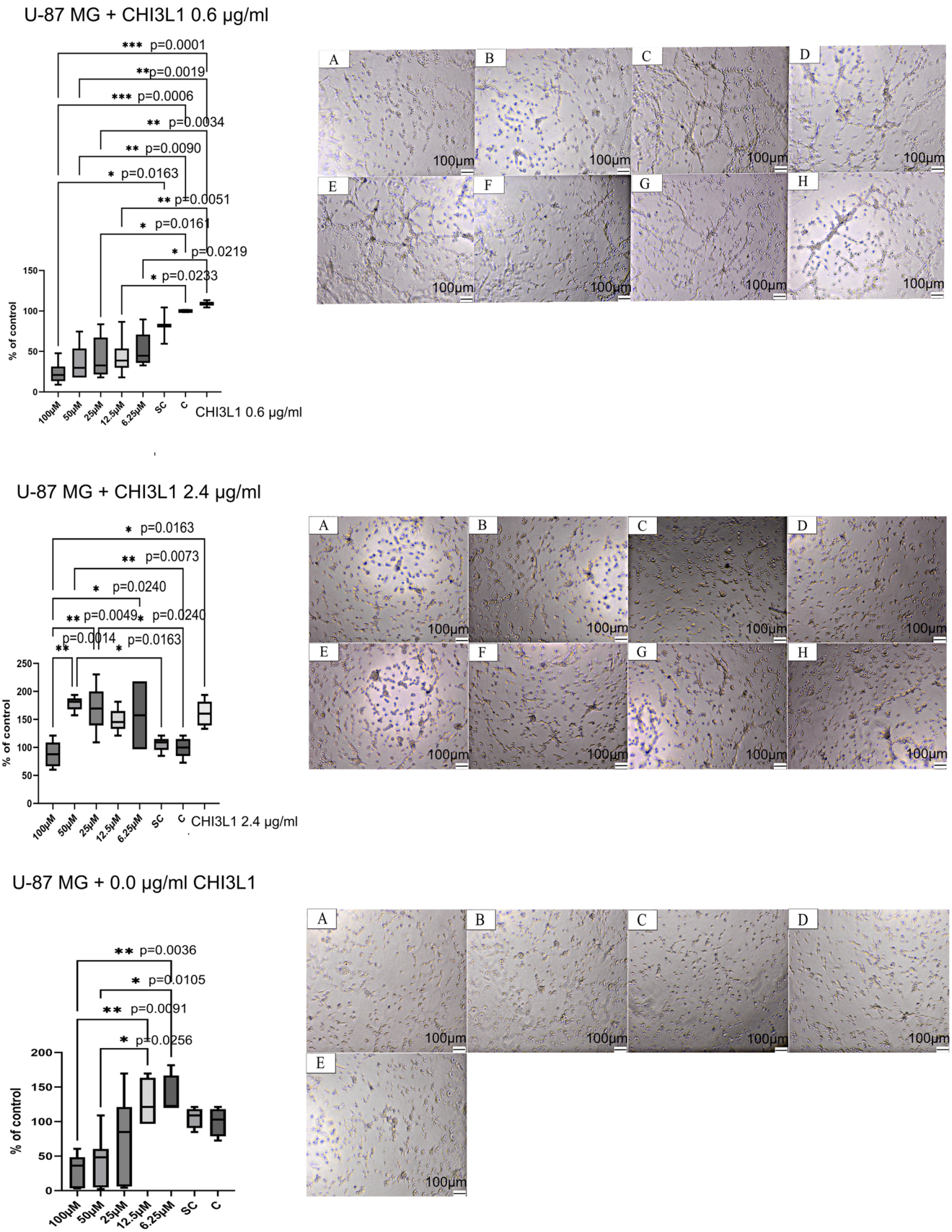

Fig. 3. Inhibition of CHI3L1-dependent vascular mimicry in U-87 MG cells. Inhibition of tube-like structure by G721–0282 in the tube formation assay with glioblastoma U-87 MG in the presence of recombinant CHI3L1 protein and CHI3L1 inhibitor: G721–0282 at five concentrations: 100 µM (A), 50 µM (B), 25 µM (C), 12.5 µM (D), 6.25 µM (E), (F) solvent control (SC; control containing DMSO concentrations found in 100 µM of G721–0282) and control (G). Control with addition of G721–0282 without CHI3L1 was included in the experiments. One-way ANOVA Tukey's post-hoc tests were performed.

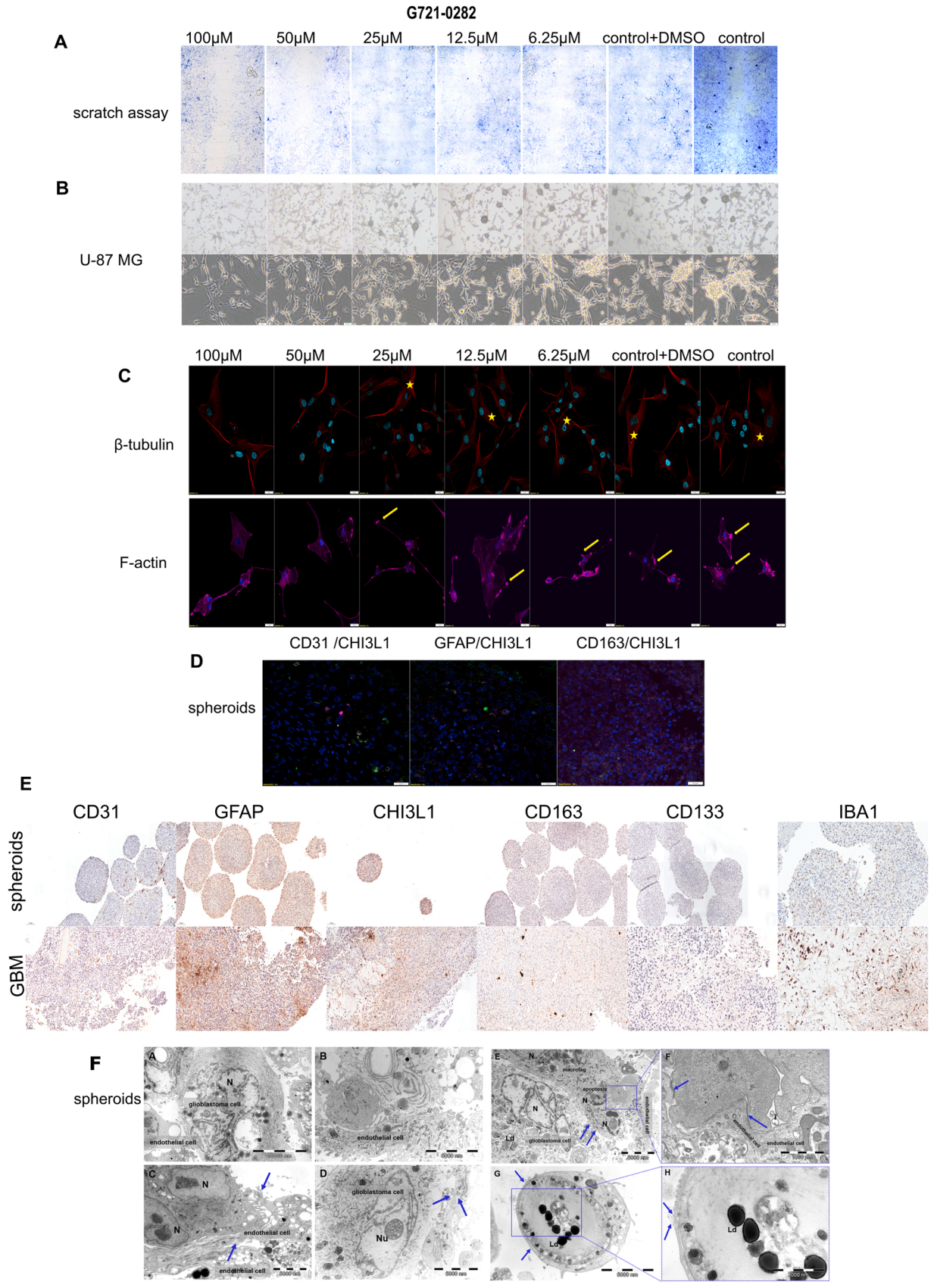

(caption on next page)

Fig. 4. Inhibition of cell migration and modification of cytoskeletal proteins as a result of CHI3L1 inhibition in U-87 MG cells, which are also component of the spheroid model used to study the effects of G721–0282. Scratch assay was performed to assess the migration of glioblastoma U-87 MG cells after G721–0282 treatment; crystal violet was used to visualise the cells -**A**. Changes in U-87 MG cells cultured in the presence of G721–0282 are shown in **B**. Cytoskeletal rearrangement after CHI3L1 inhibitor treatment was assessed in β-tubulin and F-actin visualised in the immunofluorescence reaction -**C**. Yellow stars correspond to high density of cytoskeletal β-tubulin, yellow arrows indicate phillopodia composed of F-actin philaments involved in cell motility. Control (C) with medium and control with DMSO concentrations of 100 μM of G721–0282 (SC solvent control) were included in the experiments. In the spheroid model consisting of U-87 MG cells, HMEC-1 cells and macrophages, the presence of CD31 + endothelial cells (green), GFAP- (green) and CHI3L1-positive neuronal cells (magenta) and macrophages with CD163 + phenotype 2 (green) was shown in IF reaction -**D**, IHC reaction -**E** with comparison to GBM tissue; CD133 + cancer stem cells were detected in GBM tissue and spheroids. Three cell types were also detected by TEM (**F**): A-D - different cell populations; cytoplasmic processes in C (arrows), cell-cell junctions in D (arrows). N - cell nucleus,Nu - nucleolus; E-H - electron micrographs show relationships between cells; the macrophage forms cytoplasmic processes that surround the apoptotic cells in the spheroid at E (arrows), the endothelial cell forms closing junctions at F (arrows) or surrounds another cell at G and H (arrows). N - nucleus, Ld - lipid droplets.

of this interleukin was observed at 12.5 μM. IL-6 levels were lowest at 100 μM, 50 μM, 12.5 and 6.25 μM G721–0282 compared to the solvent control group and highest at 25 μM. IL-6 levels were decreased in the solvent control group compared to the control. No differences in this interleukin level were observed in the supernatants. IL-10 levels were decreased in spheroids at 100 μM and 6.25 μM concentration of G721–0282. The highest levels of this interleukin were found at 50 μM and 25 μM. IL-10 levels in the supernatants were elevated at 6.25 μM compared to the other groups. IL-18 levels in spheroids were significantly higher at 12.5 μM. In the solvent control group, IL-18 levels were lower compared to the control group. In the supernatants only a trend towards the lowest IL-18 concentration at 100 μM was observed. In spheroids, the level of TNF-α decreased at all concentrations of G721–0282, especially at 6.25 μM, and the highest level was observed at 25 μM. In the solvent control group, TNF-α levels decreased compared to the medium control group. No differences were found in the supernatant. TNF- β expression levels in spheroids were also lowest at 6.25 μM and highest at 25 μM. In the solvent control group, the level of TNF-α increased compared to the control group. The highest level in the supernatants was at 100 μM (Fig. 5).

3.13. ddPCR

The lowest levels of CHI3L1 mRNA were observed in cells treated with 100 and 50 μM of G721–0282. CHI3L1 mRNA levels were also increased inversely with inhibitor concentration. VEGF-A mRNA level was the highest in U-87 MG cells treated with 100 μM of inhibitor and the relationship between mRNA level and compound concentration was directly proportional. The lowest levels of VEGF-A mRNA were observed in the solvent control. Conversely, in spheroids the highest levels of CHI3L1 mRNA were at 100 μM. There was no directly proportional relationship between inhibitor concentration and CHI3L1 mRNA expression, however the lowest level of VEGF-A mRNA was observed in spheroids treated with 25 μM of G721–0282. In U-87 MG cells, the highest level of VEGF-C mRNA was found at a concentration of 25 μM of G721–0282, while in a spheroid model the lowest level was found. The highest expression of VEGF-C mRNA was observed in spheroids cultured in 12.5 μM and 6.25 μM of inhibitor. No difference was observed for VEGF-D mRNA levels (Fig. 6A).

3.14. Western blotting

Western blotting showed that CHI3L1 protein increased in U-87 MG cells treated with 100 μM, 50 μM and 25 μM of G721–082. VEGF-A and VEGF-C weren't observed at the protein level, but VEGF-D expression was higher in cells treated with CHI3L1 inhibitor at concentrations of 100–12.5 μM. At 6.25 μM and control, VEGF-D levels were lowest. In cells treated with 100 μM and 25 μM G721–0282, pSTAT-3 expression was highest than in other groups and lowest in cells incubated with 6.25 μM compound (Fig. 6B).

VEGF-A expression was lowest in spheroids treated with 100 μM G721–0282. No VEGF-C protein expression was observed. VEGF-D expression was not highest in spheroids treated with G721–0282, but a concentration of 100 μM led to a decrease in this protein level. The expression of pSTAT-3 was highest in spheroids treated with 50 μM and 25 μM G721–0282. For the inhibitor concentrations studied, a decreasing influence on STAT-3 phosphorylation was observed in spheroids incubated with 100 μM G721–0282. The expression of STAT-3 was highest in spheroids incubated with 100 μM, 50 μM and 25 μM compared to the other groups (Fig. 6C). Furthermore, Western blotting analysis shows a different pattern of expression of CHI3L1, VEGFs, STAT-3 and pSTAT-3 in different types of brain tumours (Fig. 6D).

3.15. The morphological, qualitative analysis of glioblastoma single cells by DHT based digital staining

The refractive index (RI) of specific intracellular structures of glioblastoma single cells, obtained from reconstructed 3D RI tomograms, was used as an imaging contrast to visualise these structures and to perform morphological analysis of the examined single cells. The results obtained showed that the RI data obtained provided sufficient information to visualise the main intracellular structures of glioblastoma cells, which were also observed on conventional TEM images. In Fig. 7B, these characteristic structures are indicated by arrows on 2D-RI tomograms representing the central cross-section of the cells, or they are digitally coloured on 3D-RI tomograms based on their RI value. The DHT was only able to distinguish several intracellular structures in a label-free manner, including cytoplasm, nucleus, nucleoli, phagosomes and lipid droplets, based on their distinctive shapes and RI values. Visual observation of the control cells shows that the presence of the nucleus (yellow arrows and yellow staining in Fig. 7B) with multiple nucleoli is common in this cell line. The analysis of the TEM images of the examined cells showed that the nuclei are surrounded by the endoplasmic reticulum (ER), but it was not possible to distinguish the ER directly, as it has similar RI values to the nuclei. Furthermore, the presence of phagosomes in the form of low-RI vesicles in Fig. 7B (white arrows) corresponds to the TEM images of this glioblastoma cell line, which shows very high autophagy, common for this type of cancer cells. Another characteristic feature is that the nuclei are surrounded by the high RI spheroid-shaped structures (violet arrows or magenta staining in Fig. 7B).

3.16. Quantitative DHT analysis of glioblastoma single cells and intracellular structures based on RI-data

The RI data obtained allow quantitative analysis not only of the average RI values of the cells but also of the cellular structures. Firstly, based on the extracted average RI values of whole single cells from each investigated group of samples with different inhibitor concentration, it was possible to determine the statistical significance of the influence of the investigated factor: type of solvent used and inhibitor concentration on the single cells. The average RI values of the extracted cellular structures were then analysed to determine which particular structure was most affected by the inhibitor used.

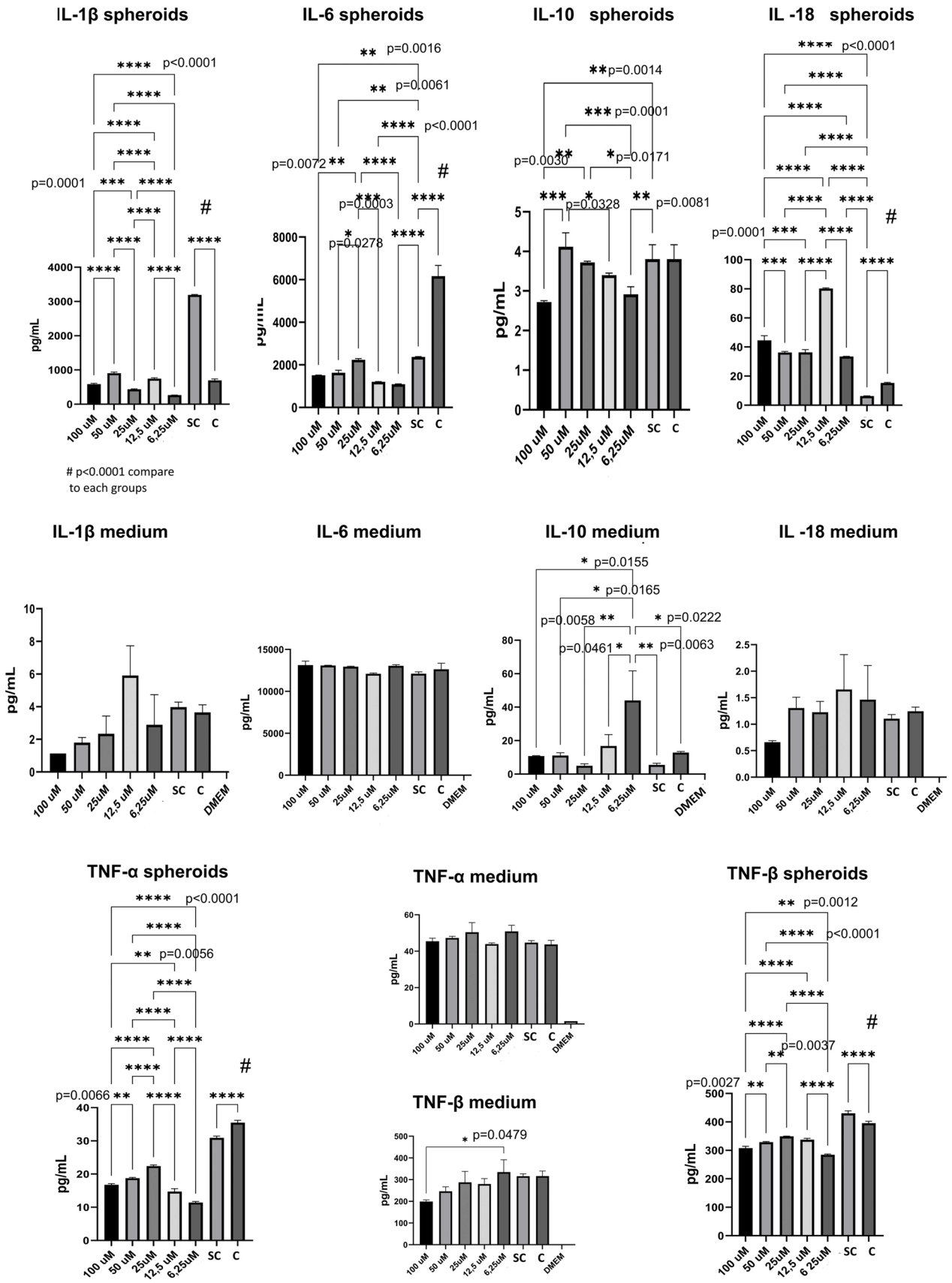

Fig. 5. Cytokine and chemokine balance after CHI3L1 inhibition. Multiplex analysis of cytokine and chemokine growth factors was performed in spheroids treated with G721–0282 and in conditioned medium from spheroid culture. A control (C) with medium and control containing DMSO concentrations equivalent to 100 μM G721–0282 (SC solvent control) was included in the experiments. One-way ANOVA Tukey's post-hoc tests for multiple comparisons were performed.

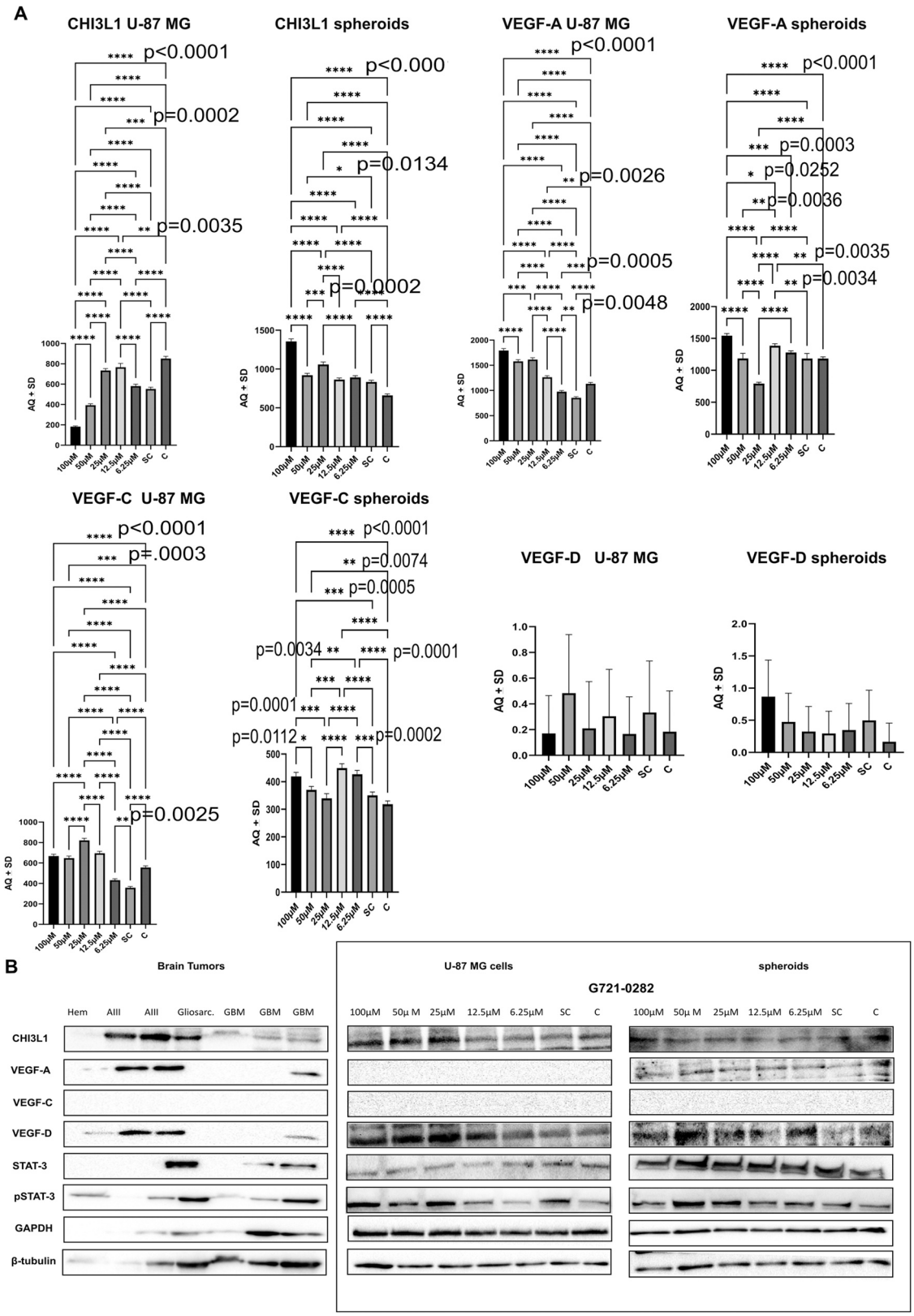

Fig. 6. Changes in mRNA and protein expression after treatment with G721–0282. Expression of mRNA levels assessed by ddPCR (**A**) in U-87 MG cells and spheroids consisting of U-87 MG cells, HMEC-1 cells and macrophages after treatment with G721–0282; A control (C) with medium and control containing DMSO concentrations occurring in 100 μM of G721–0282 (SC solvent control) was included in the experiments. One-way ANOVA Tukey's post-hoc tests were performed for multiple comparisons. Expression of protein level was performed by Western blot method (**B**) in U-87 MG cells and in spheroids after treatment with G721–0282 and also on brain tumour tissues of different grades according to WHO classification; Hem: haemangioblastoma, AIII: astrocytoma III grade, Gliosarc.-gliosarcoma, GBM-glioblastoma multiforme.

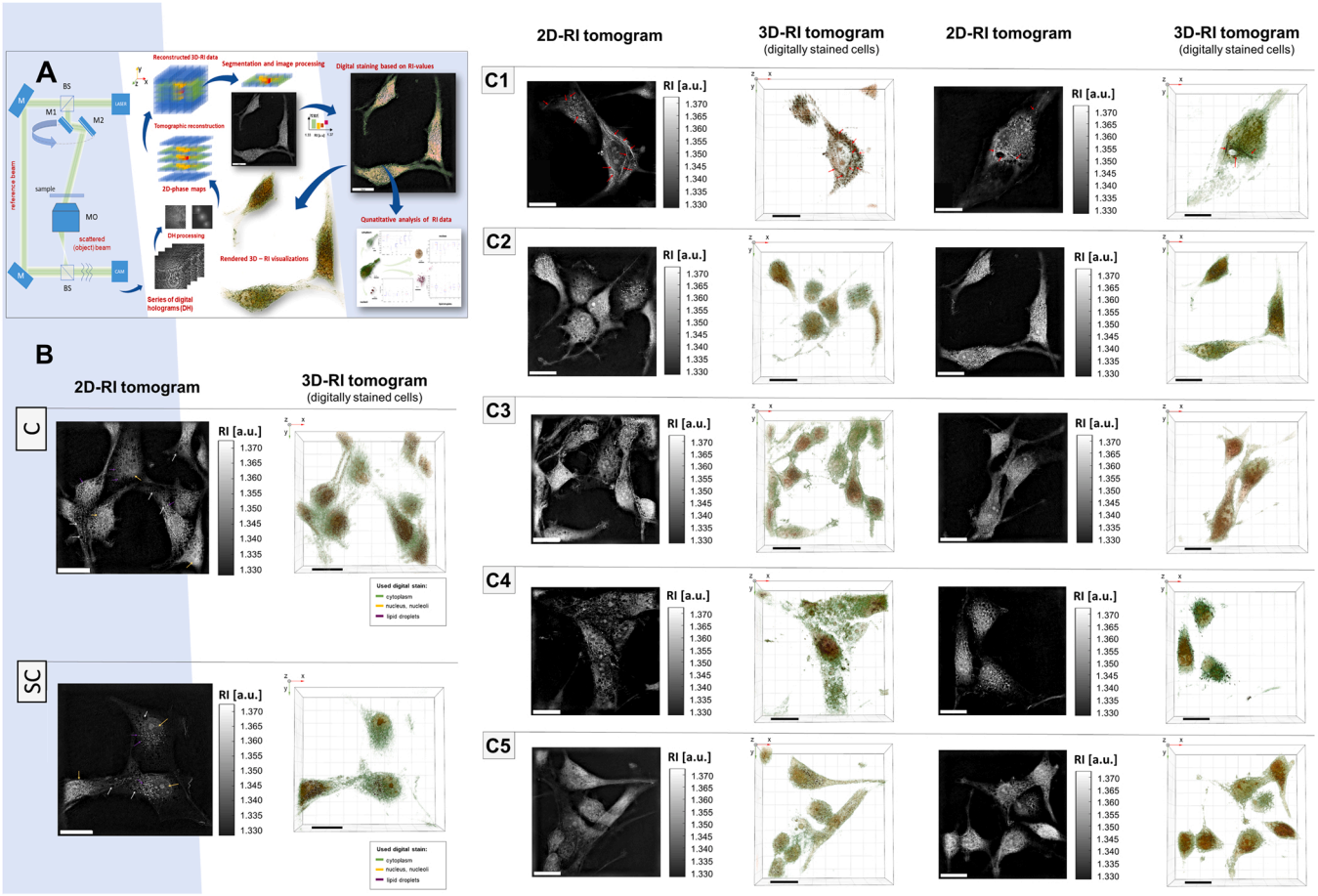

Fig. 7. Comparison of the morphological and 2D-RI distribution changes of cells after G721–0282 treatment. Scheme of the DHT study (M-flat mirrors, M1/M2-mirrors on a rotating arm, MO-microscope objective, BS-beam splitters, CAM-camera) -**A**. Representative 2D-RI tomograms and digitally stained 3D-RI tomograms of single cells untreated (control 1, control 2) and treated with inhibitor in 5 decreasing concentrations: 100 μM, 50 μM, 25 μM, 12.5 μM, 6.25 μM. White arrows indicate specific intracellular structures: white-phagosomes, yellow-nuclei with nucleoli, violet-lipid droplets, red-actin filaments. Scale bars: 20 μm -**B**.

3.16.1. The analysis of the inhibitor-induced RI changes of single cells

Fig. 8 A shows the variation in the averaged 3D-RI values of individual cells from each group examined. As there were no significant changes between C and SC samples, the average results (indicated as control) for these samples are shown in this figure. It shows that, except for the inhibitor concentration of 6.35 μM, there are significant changes between the average RI values obtained for treated and untreated (control) cells. In the case of cells treated with a concentration of 100 μM, the presence of the fibre structures (such as actin filaments) with the high RI value affects the initial range of variation of the average RI values of these cells. After eliminating these structures (100 μM modified in Fig. 8 A) from the analysis, the lowest average RI values were obtained for these cells, indicating that the greatest decrease in RI is achieved at the 100 μM concentration of inhibitor used. As the inhibitor concentration decreases, an increase in RI values is observed and at 6.26 μM the cells show the same RI as the control group.

One-way ANOVA was performed to determine the statistical significance of inhibitor concentrations on RI of single cells (see Table S1 in the Supplementary Material). First, the potential influence of the solvent used for inhibitor administration on the cells was analysed by comparing the control group and the group of cells incubated with the solvent. The determined p-value (Prob>F) for the F-statistic is higher than the assumed significance level (in our case 0.05), which indicates that the solvent used has no significant influence on the RI values of the examined cells.

Furthermore, the other ANOVA results show the existence of the statistically significant differences in the average RI values of the cells only for the inhibitor concentrations from 100 to 12.5 μM. The lowest p-value indicating the most significant variation in RI values between the control and tested groups, was initially not obtained for the highest concentration of 100 μM (without modification), but for the 50 μM concentration.

The lowest RI values obtained at a concentration of 50 μM indicate the lower density of the inhibitor treated cells compared to the control cells, which may be related to the lower concentration of the proteins in the cytoplasm. As the inhibitor concentration is decreased, an increase in the averaged RI values of the cells is observed, so that at a concentration of 6.25 μM, no statistically significant changes in RI were observed between the treated and control cells. It should be noted, however, that such a result for the 100 μM concentration may be related to already indicated the presence of actin filament like structures, as already indicated, which exhibit higher RI values and affect the averaged RI values of these cells. After eliminating these structures from the analysis, the average RI values for this group decreased significantly and the most significant differences between the control cells and treated cells were indicated by ANOVA for the 100 μM concentration, confirming that the increase in inhibitor concentration leads to a decrease in the average 3D-RI of the single cells and a decrease in their intracellular density.

3.16.2. The analysis of the inhibitor-induced RI changes of cellular structures

To investigate possible inhibitor concentration-dependent changes at the intracellular level, the average RI values of some specific structures

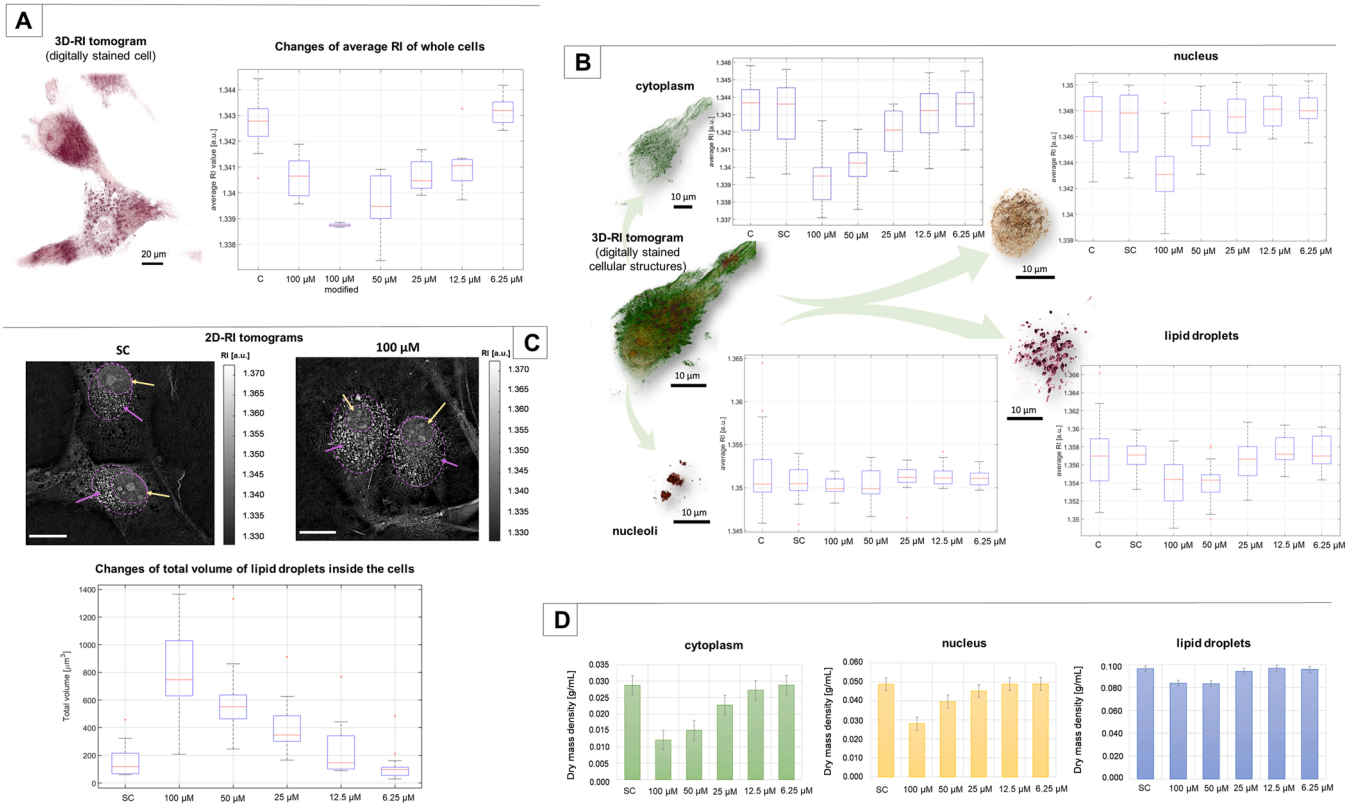

Fig. 8. Quantitative analysis of RI data based changes in single cells and cellular structures after G721–0282 treatment. The exemplary 3D-RI tomogram of a digitally stained single cell and the boxplot representing the variation of the average RI values of single cells among different groups of samples examined (untreated: C, SC, treated: 100–6.25 µM) - **A**. The representative digitally stained cellular structures (cytoplasm, nucleus, nucleoli, lipid droplets) based on RI values and boxplots of their average RI values in the presence of different concentrations of the inhibitor (100–6. 25 µM) - **B**. The study of the presence of lipid droplets inside the single cells: the exemplary 2D-RI tomograms of control 2 and 100 µM samples (yellow arrows indicate the nucleus with nucleoli, violet arrows indicate the lipid droplets in the region surrounding the nucleus) and boxplot representing the variation of the total volume of lipid droplets inside the cells. Scale bars: 10 µm - **C**. The changes in the determined dry mass density of the cytoplasm, nucleus and lipid droplets of the control 2 samples and the samples with five different concentrations of inhibitor (100–6.25 µM). - **D**.

were examined. The ability to differentiate intracellular structures based on RI values has been demonstrated previously [67].

The variation in RI of intracellular structures provides insight into physiological and externally induced changes in the density of these structures caused by changes in the concentration of chemical components. However, it should be noted that their differentiation is directly related to the ability to distinguish the minimal local variation of RI. In our case, on the basis of the digitally stained cells, it was possible to analyse the variation in the average RI values of intracellular structures such as the cytoplasm, nucleus, nucleoli and lipid droplets caused by the decrease in the inhibitor concentration from 100 to 6.25 µM, compared to the variation between the reference cells (control1/control2). The results are shown in Fig. 8B.

In the case of all the cells analysed among the reference samples, the median values of the average RI values of all the structures are similar, indicating that the solvent used for the administration of the inhibitor did not affect the intracellular structures.

It can be seen that increasing the inhibitor concentration leads to a decrease in the average RI value of the cytoplasm, indicating a decrease in its optical density, which may be associated with significant changes in the intracellular protein concentration, including cytoskeletal proteins. One-way ANOVA (see Table S2 in the Supplementary Material) indicates the existence of statistically significant differences only between Control 2 and 100, 50, 25 µM inhibitor-treated samples. The differences in the average RI values of the cytoplasm decrease with decreasing inhibitor concentration and for 12.5 and 6.25 µM there are no statistically significant differences between control and inhibitor-treated cells. The significant decrease in average cytoplasmic RI values may be related to the reorganisation of the cytoskeletal structure of these cells induced by the high inhibitor concentration, as indicated by the presence of high RI actin fibre-like structures (average RI equal to 1.360276). In the case of cells from other groups of samples (50–6.25 µM), there were no counterparts of such structures inside them. In the case of cells treated with 50 µM, which have a higher average RI of the cytoplasm, it is possible that the concentration of inhibitor used limits the concentration of proteins, leading to a decrease in the density of the cytoplasm, but without the presence of these fibre-like structures as in the case of cells treated with 100 µM. This effect suggests that the 100 µM concentration is the one that most alters the dynamics of cytoskeletal proteins.

In the case of one nucleus (see Fig. 8B), the statistically significant decrease in its average RI values was only observed at the 100 and 50 µM concentration, with the highest decrease also observed at the highest inhibitor concentration (100 µM). The results of the one-way ANOVA indicate that at lower concentrations (25–6.25 µM), the average RI of the nucleus did not show statistically significant differences between inhibitor-treated and reference cells (see Table S2). Taking into account the resolution of DHT and the previously indicated presence of the annulus-like structure of rough endoplasmic reticulum (rER) or granular endoplasmic reticulum closely surrounding the nuclei of the glioblastoma cells examined, the peripheral regions of the nuclei may also contain rER. It was not possible to fully extract this structure for the nucleus, which may affect the results obtained. The inhibitor may affect the concentration of proteins synthesised within the rough endoplasmic

reticulum, leading to a decrease in the average RI values of the regions extracted from the 3D RI tomograms as nuclei. As in the previous cases, the most significant decrease in RI is observed at the highest inhibitor concentration (6.25 μM).

In the case of glioblastoma cell nucleoli, the concentrations of inhibitor used (100–6.25 μM) did not statistically affect their mean RI values. The median RI values are almost the same in all cases (see Fig. 8B), which was also confirmed by one-way ANOVA (see Table S2).

In the case of lipid droplets, the results were similar to those obtained for the nucleus (see Fig. 8B). The decrease in their average RI value, which led to statistically significant differences between the reference and inhibitor-treated cells, was observed only in the case of the 100 and 50 μM concentrations. These results suggest that the inhibitor used may affect the concentration of these types of proteins in the lipid droplets, but this process is directly related to the inhibitor concentration. The ANOVA results (see Table S2) indicate that the decrease in protein concentration in lipid droplets was statistically significant only for 100 and 50 μM inhibitor concentrations.

Visual observation of the reconstructed 3D RI tomograms showed that the number of lipid droplets was significantly higher in the inhibitor-treated cells than in the control 2 cells (see Fig. 8 C). Based on the digital staining of the lipid droplets, it was possible to compare the total volume of lipid droplets in the cells of all samples examined. The results show that the total volume of lipid droplets inside the cells increases as the concentration of inhibitor used increases.

For a more complex analysis of the inhibitor-induced changes in protein concentration within the examined cells, the dry mass density was determined based on the extracted RI values of the cytoplasm, nucleus and lipid droplets (see Fig. 8D). As can be seen in the case of the cytoplasm, the differences in dry mass density between control 2 and inhibitor-treated cells were 0.00167, 0.0137 and 0.0060 g/ml for the concentrations of 100, 50 and 25 μM, respectively. This confirms that the use of the higher concentrations of inhibitor leads to the greatest decrease in protein concentration in the cytoplasm. In the case of the nucleus, the same tendency occurs; the differences in dry mass density were equal to 0.0207, 0.0091 g/ml for the concentrations of 100 and 50 μM, respectively. Therefore, the highest difference in dry mass density was obtained for the reference and inhibitor-treated (100 μM) samples for the nuclei. These values were an order of magnitude higher than those for the cytoplasm, but the nucleus and the surrounding endoplasmic reticulum can have a higher protein concentration than the cytoplasm, which could be responsible for the higher changes in dry mass density for the highest inhibitor concentration. On the other hand, for the lipid droplets with the highest RI values, the differences in dry mass density were 0.01267 and 0.0130 g/ml for 100 and 50 μM concentrations, respectively. Therefore, the greatest decrease in protein concentration was obtained at the 50 μM concentration, which is also confirmed by the previous results of the ANOVA (see Table S2), where the lowest p-value was obtained for this concentration of inhibitor. These results indicate the strongest effect of G721–0282 at 100 μM and 50 μM.

4. Discussion

The cytotoxicity evaluation of G721–0282 performed on glioblastoma U-87 MG cells expressing CHI3L1, as well as on normal endothelial cells HMEC-1 and NHDF fibroblasts, which do not express this protein, showed that the at-IC50 value was not reached. The cytotoxic effect of G721–0282 on these cells was not investigated. To our knowledge, the cytotoxic potential of G721–0282 on cancer cells has only been investigated on the human osteosarcoma cell lines MG-63 and U2OS by Park et al. and these results show decreasing cell viability depending on concentration and time [12]. Our results indicate that G721–0282 doesn't have a high cytotoxic potential for normal endothelial cells and fibroblasts and suggest the possibility of selective interactions of G721–0282 limited to CHI3L1 inhibition without a broad non-specific cytotoxic effect. Our results are in agreement with the article published by Ham et al., where the authors presented no cytotoxic potential on BV-2 murine microglial cells in the concentration range of 5, 10 and 20 μM [68]. Results obtained from the analysis of cell cycle, apoptosis and necrosis in U-87 MG cells treated with CHI3L1 inhibitor also confirm that this compound did not cause a direct cytotoxic effect, but some cell cycle alteration was observed. These results indicate that the main molecular mechanism of CHI3L1 inhibition has biological potential in various fields. In addition, these results suggest that the activity of G721–0282 may be more selective and less toxic, which is critical in the treatment of GBM. Currently, the standard chemotherapeutic agent used to treat GBM is temozolomide, the main side effect of which is haematological toxicity. Treatment with bevacizumab, which is used as an anti-angiogenic agent by blocking VEGF-A, also often leads to leukopenia and hypertension. In fact, the efficacy of standard treatment, including adjuvant and neoadjuvant regimens, in GBM is still inadequate and overall patient survival is limited to a few months [69]. From this point of view, screening for new agents with antitumour activity and less systemic toxicity is urgently needed to improve the treatment of GBM.

In a recent study, novel non-contact, non-destructive and label-free digital holographic tomography (DHT) was used to characterise G721–0282 inhibitor-induced changes in glioblastoma cells, their motility and adhesion. It was the first attempt to use this technique to quantitatively study inhibitor-induced changes at the single cell level based solely on reconstructed RI data without the use of exogenous markers. Our DHT results showed a decrease in cytoplasmic density of U-87 MG cells at the two highest concentrations of G721–0282 and also the formation of protein fibres. We believe that this may be an effect of altered depolymerisation of actin fibres and may explain the decrease in cell motility observed in the scratch assay. We also observed a similar effect of G721–028 on cytoskeletal modifications by immunofluorescence visualisation of F-actin and β-tubulin fibres, resulting in reduced actin and tubulin fibre density, abnormal polymerised fibre architecture and phillopodia development. Altered motility of cancer cells has the potential to reduce invasiveness and is a promising effect in anti-cancer treatment. Recently, a similar effect was observed by Bartak et al. [70] and was obtained by treating glioblastoma A172 cells with Alphaherpesvirus. Infected cells were shown to have impaired migration due to rearrangement of the actin cytoskeleton. The presence of similar changes in the actin cytoskeleton network as internal and peripheral actin stress filaments suggests that the use of the proposed inhibitor at a concentration of 100 μM may lead to the same effects as in the case of Alphaherpesvirus, a potential oncolytic virus for cancer therapy [70]. In DHT imaging, we also observed an increase in the volume of lipid droplets together with a decrease in their density in the two highest concentrations of G721–0282 in U-87 MG cells, and these effects could probably be explained by an alteration in lipid management caused by the inhibitor used. At present, lipidomic analysis of this effect appears to be another avenue of research worth exploring. Previously reported results indicate that the lipids in cells have significantly higher RI values than the cytoplasm [20], [29]. Therefore, the obtained DHT and TEM results suggested that these structures are the lipid droplets, which are a spheroid-shaped monolayer enclosing phospholipid and associated proteins. In general, they were located close to the nuclei and the surrounding ER, which confirms our observation, since the common hypothesis of lipid droplet biogenesis considers lipid droplets as ER-derived organelles [71]. Since lipids have significantly higher RI values than cytoplasm and other organelles in cells [29], the 3D RI distribution of lipid droplets can be effectively segmented from the surrounding cytoplasm. Previously reported results verified the colocalisation of digitally-stained intracellular lipid droplets based on their RI values and Nile Red-stained lipid droplets [22]. In addition, lipid droplets are generally located in the perinuclear region, which may be related to the presence of the ER in this region. Lipid droplets act as hubs that coordinate the pathways of lipid uptake, distribution, storage and

utilisation in the cell. They are also essential components of the cellular stress response [72–76]. They are generally spherical organelles consisting of a core and a single phospholipid membrane. The core of the lipid droplet contains mainly triacylglycerols. However, the lipid droplet membrane binds many proteins that may have functions unrelated to lipid metabolism. The major family of proteins associated with lipid droplets are the PAT proteins (perilipin, ADRP and TIP 4), which are responsible for regulating lipid metabolism [71]. However, lipid droplets in a variety of cell types may also contain proteins with well-established roles in the pathogenesis of inflammation and oncogenic cell transformation, tumourigenesis and metastasis, including PI3K, ERK1, ERK2, p38, PKC and caveolin. Indeed, increased lipid droplets play a role in tumour cell resistance to the therapeutic agent due to sequestration, and a correlation with ERK/Akt/mTOR pathway activation has been observed with this phenomenon [77]. Furthermore, lipid droplets have been implicated in a wide range of carcinogenesis through their involvement in the activation of angiogenesis, metastasis, invasion, cell cycle progression and immunomodulation of the microenvironment. One of our hypotheses is that this effect is related to the stress induced by G721–0282 in U-87 MG cells, and this effect is the focus of our further analysis. These results could potentially indicate an alteration in lipid accumulation induced by the inhibitor, however this effect should be further verified as this effect of G721–0282 has not been previously studied. Higher levels of perilipins were observed in glioblastoma tumours. Increased lipid droplets are considered a poor prognostic factor in many cancers and inhibitors of their formation are being considered as a targeted therapy in glioblastoma [78,79]. To the best of our knowledge, this paper is the first to demonstrate the effect of G721–0282 on interleukin expression. Multiplex analyses show that G721–0282 has a general potential to reduce IL-1β levels. Interestingly, this effect was not linearly dependent on compound concentration. Western blotting analysis showed that the pSTAT-3 expression pattern was similar to IL-1β levels in spheroids treated with G721–0282. These experiments show that the effect of CHI3L1 inhibition, although mainly in U-87 MG cells, was model dependent and therefore different STAT-3 phosphorylation could be observed as a result. The levels of IL-1β secreted into the medium confirmed these trends. The results obtained by our team are important in terms of the potential of IL-1β. This cytokine is known to promote pro-tumour mechanisms in gliomas by orchestrating inflammation, and high levels of this interleukin are associated with poor prognosis: correlation with progression and shorter overall survival of patients. Higher IL-1β expression has also been reported in GBM (WHO grade IV) compared to glioma tumours of histological grades II and III [80]. Recent work by Kai's team shows that IL-1β expressed in glioblastoma and by tumour-associated macrophages (TAMs) promotes tumour growth through the STAT-3/Nf-KB pathway [80]. This suggests that anti-IL-1 β therapy could be considered in the treatment of glioblastoma due to this interleukin effect on tumour growth [81]. In this context, our results are promising as G721–028 significantly reduced the effect of IL-1β in glioblastoma spheroids.

We also observed a significant decrease in IL-6 levels in spheroids after treatment with G721–0282. Interestingly, the effect of G721–0282 was also not proportional to concentration and a strong effect was observed at low concentrations. A similar effect of G721–0282 was observed on pSTAT-3 expression in U-87 MG cells by Western blotting. This relationship of pSTAT-3 expression was not as clear in spheroids treated with G721–0282. These results may suggest that G721–0282 reduces IL-6 expression through inactivation of STAT-3 phosphorylation and acts mainly in glioblastoma U-87 MG cells, which are a sensitive component of spheroids for this inhibitor due to CHI3L1 expression. In the case of IL-6 levels in the supernatants of spheroids treated with G721–0282, we didn't observe any significant changes, probably because this interleukin efflux did not occur effectively. This cytokine plays an important role in the immunomodulatory process that occurs during cancer development. IL-6 plays a critical role in immunosuppression in glioblastoma by polarising macrophages and orchestrating and regulating immunological responses through Jak/STAT-3 activation [82], [83]. Higher levels of IL-6 in CSF and serum increase with glioma grade. Promising results from in vivo studies by Yang et al. suggest that reducing IL-6 levels is an important target for antibody-based immunotherapy in the treatment of GMB. The therapeutic effect of this therapy works by increasing the infiltration of T cells with positive expression of CD3, CD4 and CD8, reversing macrophage polarisation and improving the survival of tumour-bearing mice [83]. We also observed a significant decrease in IL-6 levels in spheroids after treatment with G721–0282. Interestingly, the effect of G721–0282 was also not proportional to concentration and a strong effect was observed at low concentrations. A similar effect of G721–0282 was observed on pSTAT-3 expression in U-87 MG cells by Western blotting. This relationship of pSTAT-3 expression was not as clear in spheroids treated with G721–0282. These results may suggest that G721–0282 reduces IL-6 expression through inactivation of STAT-3 phosphorylation and acts mainly in glioblastoma U-87 MG cells, which are a sensitive component of spheroids for this inhibitor due to CHI3L1 expression. In the case of IL-6 levels in the supernatants of spheroids treated with G721–0282, we didn't observe any significant changes, probably because this interleukin efflux did not occur effectively. This cytokine plays an important role in the immunomodulatory process that occurs during cancer development. IL-6 plays a critical role in immunosuppression in glioblastoma by polarising macrophages and orchestrating and regulating immunological responses through Jak/STAT-3 activation [82], [83]. Higher levels of IL-6 in CSF and serum increase with glioma grade. Promising results from in vivo studies by Yang et al. suggest that reducing IL-6 levels is an important target for antibody-based immunotherapy in the treatment of GMB [83]. The therapeutic effect of this therapy works by increasing the infiltration of T cells with positive expression of CD3, CD4 and CD8, reversing macrophage polarisation and improving the survival of tumour-bearing mice [83].

In fact, the solvent control showed a different effect than the control, as DMSO is known to have anti-inflammatory and immunomodulatory effects [84], [85]. Therefore, changes in cytokine levels involved in inflammation was observed in DMSO-treated spheroids. In this experiment we also want to compare the changes caused by DMSO and G721–0282 at a concentration of 100 μM. Reduced levels of cytokines such as IL-1β, IL-6 or IL-10 in spheroids treated with the highest concentrations of G721–0282 indicate that this compound acts despite the presence of DMSO. A similar effect of G721–0282 was also observed for IL-18, where a significantly higher cytokine level was observed compared to the solvent control: G721–0282 works despite the presence of DMSO.

Our results are consistent with current knowledge that CHI3L1 expression is associated with levels of interleukins and factors. According to Ahangari et al. an experiment performed in a mouse model of asthma showed that higher CHI3L1 levels are associated with higher IL-1 β, IL-6, IL-10 and TNF-α expression and in CHI3L1 knockout mice the levels of these factors were significantly lower compared to the wild type [86]. These relationships between CHI3L1 and factors could also be found in our results.

It is worth considering that interleukins are expressed not only by tumour cells but also by macrophages and disturb the balance between these factors, which will have a different effect in the spheroid model, which is closer to the real tumour, where some compensatory effects in the microenvironment may develop. Another important point is that interleukins act in a network where balance is important.

Next, our results show that the IL-10 levels detected in the spheroids were reduced with the concentration of G721–028. In Western blot analysis, we observed that pSTAT-3 expression in spheroids decreased in the same way, which may indicate that this mechanism of G721–0282 in IL-10 decrease acts via changes in STAT-3 phosphorylation. The expression of pSTAT-3 in U-87 MG cells was also lowest at 6.25 μM. This suggests that low concentrations of G721–028 effectively inactivate STAT-3 phosphorylation and also affect interleukin expression. IL-10 is

known to be a pro-tumour factor in glioblastoma, but the influence of IL-10 levels on overall survival of patients with GBM is not clear, although there is evidence for its higher expression in GBM IV and III compared to grade II [69]. The main pro-tumour effect of this interleukin is described as stimulation of proliferation, angiogenesis, migration and invasion. IL-10 is also an important factor in immune escape and the main source of IL-10 are TAMs and also glioma CD133 + stem cells [69]. Increased IL-10 expression and glioma-associated macrophages are associated with the invasive phenotype. Mechanistically, IL-10 acts in GBM through activation of JAK/STAT-3 [87]. In addition, Zadka and co-workers have shown higher levels of IL-10 receptor expression in primary brain tumours compared to metastases, suggesting a role for receptors in glioblastoma progression [88].

Our results are consistent with these findings and suggest promising anti-tumour effects of G721–0282. Recent studies have shown that blocking IL-10Rα is being considered as an effective treatment in breast cancer [89]. However, in glioma, the role of IL-10 is still unclear, and immunostimulatory and anti-tumour effects on CD4 + and CD8 + T cells are also described, as if there were direct effects of this interleukin. These phenomena complicate anti-GBM immunotherapy based on IL-10 treatment [69].

Differences between Western blot results in pSTAT-3 expression levels between U-87 MG cells and spheroids may be due to the influence of the tumour microenvironment in these spheroids composed of endothelial and macrophage cells, but pSTAT-3 levels in U-87 MG cells directly explain the effect of CHI3L1 inhibition in these cells. Interestingly, the level of IL-10 secreted into the medium from spheroid culture was inversely related to the level in spheroid lysates, and this effect could probably be explained by efflux of this interleukin into the medium. The mechanism of G721–0282 in reducing STAT-3 phosphorylation was first described by Park et al. [12] in an in vitro study using the human osteosarcoma cell lines MG63 and U2OS, which also express CHI3L1. Our study confirms that G721–0282 acts through the pSTAT-3 pathway and shows this effect for the first time in human glioblastoma U-87 MG cells. Furthermore, our results show a significant increase in IL-18 expression influenced by G721–0282. This trend was also observed at the level of cytokines secreted into the medium. IL-18 has a strong proinflammatory and pleiotropic potential and acts mainly by throwing induction of IFN- expression by Th1 lymphocytes and NK cells in the presence of IL-12 [90]. *In vivo* experiments conducted on murine models of melanoma indicate that administration of IL-18 has anti-tumour effects and is promising in reducing tumour metastasis, especially in combination with immune checkpoint PD-1 neutralisations [90],[91]. Beneficial effects of IL-18 on melanoma tumour regression in mice by engineered T cells were presented by Kunert et all. In this paper, the authors also point out the non-toxic systemic side effects of this treatment [92]. Administration of IL-18 has been investigated in phase I clinical trials in patients with melanoma, renal cancer and Hodgkin's lymphoma, showing partial responses with acceptable toxicity [93]. However, the role of IL-18 in GBM is still unclear. It is considered a poor prognostic factor in GBM, stimulating angiogenesis, regulating VEGF expression and increasing metastasis [94]. On the other hand, anti-tumour activity has been suggested in a mouse model of glioma [95], so this line of research is worth pursuing.

In our experiments, G7821–028 had similar effects on TNF-α and TNF-β, significantly reducing the expression of these factors. TNF-α is known to have anti-inflammatory and anti-tumour properties and to orchestrate a broad immune response [96], [97]. However, there is also strong evidence that TNF-α expression in malignant cells and the tumour microenvironment promotes angiogenesis, invasion and TAM polarisation. Clinical trials with TNF-α antagonists show clinical benefit in ovarian and renal cancer [97], [98]. In addition, some studies suggest a beneficial role of TNF-α antagonists in in vivo models of breast cancer and fibrosarcoma [99], [100]. In this regard, the influence of G721–0282 in reducing TNF-α could be considered a promising area for further research.

On the other hand, TNF-β, which has been less studied than TNF-α, is an anti-inflammatory factor. *In vivo* studies in murine glioblastoma suggest that blocking TNF-β may be effective in combination treatment against tumour invasiveness [101]. In this context, TNF-β agonist therapy has been considered as potentially clinically relevant in reducing the immunosuppression induced by TAMs [69]. However, clinical trials in glioma and glioblastoma patients with TNF-β receptor inhibition have shown no benefit [102], [103]. Our results showed a significant decrease in TNF-β expression for all concentrations of G721–0282 and especially for the lowest concentration of this compound. It is worth investigating further whether this result, together with another cytokine balance induced by G721–0282, has a positive impact on glioblastoma regression. Indeed, the influence of G721–0282 on the expression of various factors has not yet been reported by other authors.

In general, the effect of CHI3L1 inhibition on cytokine balance is mediated via decreased levels of the pro-inflammatory IL-1β, Il-6 and TNF-α, and also decreased immunosuppressive IL-10 and TNF-β. Only IL-18, which is considered a pro-inflammatory cytokine with orchestrated potential to moderate other cytokine and growth factor levels, is increased after G721–0282 treatment. This result suggests a specific and complementary effect of G721–028 in our in vitro model of glioblastoma with CHI3L1 expression. Involvement of CHI3L1 in GBM immunomodulation and support of M2 macrophage infiltration has also been reported by Chen et al. in an in vitro and in vivo mouse model of glioblastoma via activation of the PI3K/Akt/mTOR axis; CHI3L1 appears to play a critical role in the immune escape of GBM [104].

Our team's experiments were performed using a spheroid model composed of three cell types found in brain tumours: glioblastoma cells, microvascular cells and macrophages. Glioblastoma tumours are rich in vessels due to the high vasculogenic activity of the tumour microenvironment, and macrophage infiltration occurs up to 40% of tumour mass and is involved in the cross-talk between immune response and angiogenesis. It is currently believed that spheroids are generally more physiological models of tumours than traditional monolayer culture; the multiculture spheroid model better reflects the microenvironment of solid tumours. Several spheroid models of glioblastoma have been described in the literature [105], [106]. Recently, a vascularised tumouroid model of GMB composed of glioblastoma cells, HUVEC (human umbilical microvessel cell line) and dermal fibroblast cells used in angiogenesis studies was described by Tatla [107]. In our spheroid design, we chose to include glioblastoma cells, macrophages and vascular endothelium, which we believe may better reflect the complex interactions that occur in glioma tumours compared to a model limited to U-87 MG cells, and the response to CHI3L1 inhibitor in the presence of a microenvironment more closely resembles the in vivo model. It is well documented that cross-talk between tumour cells and the microenvironment is involved in the response to anti-tumour therapy and should be considered in the design of targeted therapies. In addition, TEM micrographs revealed cell interactions and connections, confirming that the functions of the spheroids are similar to those of glioblastoma tumours. The spheroid model used in this study consists of macrophages derived from THP-1 monocytes and they are not identical to microglia, however, positive immunohistochemical reactions for antigens characteristic of GBM were observed in the spheroids for GFP, IBA1, CD31 and also for CD133. These results indicate the relevance of using this type of spheroids as an in vitro model of GBM. To date, none of the CHI3L1 inhibitors have been tested in the glioblastoma spheroid model, which could be seen as a step between cell culture research and the in vivo model of human glioblastoma.

In addition, our theoretical *in silico* modelling showed that G721–0282 can penetrate the blood-brain barrier. It is promising due to the fact that one of the challenges in GBM treatment is BBB exclusive generate problem with drug delivery [1]. However, the pharmacokinetics of this compound is not known and should be established in future research. Currently in publications are presented interactions of CHI3L1 and G721–0281 only in model docking [12], however, calculation of

BBB permeation when this compound we present for the first time.

The ddPCR assay showed that G721–0282 caused a concentration-dependent decrease in CHI3L1 mRNA expression and an increase in VEGF-A mRNA expression in U-87 MG cells. This effect could be explained by a compensatory role of VEGF-A and CHI3L1 due to their both pro-angiogenic roles. Similar observations were presented by Francescone and co-workers, where the authors showed that blocking VEGF for one week in U-87 MG and SNB75 glioma cells stimulated CHI3L1 expression at protein and mRNA levels, and also that VEGF doesn't have the potential to regulate CHI3L1 expression, but that CHI3L1 regulates VEGF [7]. The results obtained by Francescone's team were obtained using anti-VEGF antibodies. Our results showed the potential of G721–0282 for a biological effect comparable to specific antibodies. Interestingly, in spheroids the effect of CHI3L1 was reversed, leading to an increase in CHI3L1 mRNA and also an increase in VEGF-A mRNA at the highest concentration of inhibitor. This may be explained by compensation of the CHI3L1 inhibition and also indicates that G721–0282 leads to a decrease in the most important pro-angiogenic factor: VEGF-A. Furthermore, the increased expression of CHI3L1 proteins in U-87 MG cells treated with the highest concentrations of G721–0282 suggests a compensatory mechanism of CHI3L1 overexpression after loss of this protein activity, confirming the occurrence of specific inhibition. These results are important in view of the pro-angiogenic switch and resistance to anti-angiogenic therapy observed in the treatment of GBM patients [7]. However, the future perspective is to investigate the combined effect of both CHI3L1 and VEGF-A inhibition. Furthermore, in our experiments we observed that G721–0282 increased the expression of VEGF-A mRNA in U-87 MG cells, whereas VEGF-A protein was not detectable. It should be noted that U-87 MG cells were not cultured under hypoxic conditions, so proteins characteristic of this condition, such as VEGF-A or HIF-1α, could not be detected at the protein level. In spheroids, VEGF-A was detectable as a protein, because in this model hypoxia could be present inside the spheroids.

It is also interesting that the change in VEGF-C mRNA was reversed after G721–0282 treatment in U-87 MG cells. This may be relevant in partially angiogenic and lymphangiogenic diseases. However, VEGF-D mRNA levels appear to be insensitive to CHI3L1 inhibition in both cell and spheroid models. To our knowledge, the effect of CHI3L1 inhibition on VEGF-C and VEGF-D mRNA levels has not been investigated. Analysis of protein levels by Western blotting showed increased VEGF-D expression in U-87 MG cells treated with G721–0282. In spheroids, a variable effect of VEGF-A and VEGF-D was observed, but VEGF-C was not detectable. It is likely that this effect is more pronounced in hypoxic culture conditions, which induce VEGFs more efficiently. On the other hand, in GBM tumours, the expression of VEGFs is variable during tumour development and different in tumours of some types, which we also present in Western blotting performer on human tissue samples. Mechanistically, inhibition of CHI3L1 by G721–0282 resulted in increased STAT-3 phosphorylation in U-87 MG cells and also in spheroids, but in a different manner. Altered activation of this pathway may be involved in all biological effects of CHI3L1 inhibition. In our study, we observed that G721–0282 decreased CHI3L1 mRNA expression and also increased CHI3L1 protein expression in U-87 MG cells. This could be the exact effect of specific CHI3L1 inhibition. The presence of the protein may be highest after the addition of the inhibitor because compensatory mechanisms occur in the cells that provide the highest protein levels of CHI3L1. In general, inhibition leads to the deactivation of the protein rather than a reduction in its levels. Decreased levels of CHI3L1 mRNA indicate an inhibitory effect of G721–0282, but changes in protein expression show a second line of this effect, which could be explained by the cells' response to CHI3L1 deactivation.

The results obtained by our team showed inhibition of tube formation by HMEC-1 in the presence of recombinant CHI3L1 protein and G721–0282, clearly demonstrating the anti-angiogenic effect of this compound. This is the first time that this CHI3L1 inhibitor has been investigated for its reported anti-angiogenic properties. In addition, the inhibition of tube-like structures known as vascular mimicry, which occurs in various tumour types by G721–0282, was also observed for the first time in U-87 MG cells. However, the direct effect of the recombinant protein and inhibitor interactions could be modified by the natural presence of CHI3L1 expression in U-87 MG cells. Our results show that the endogenous expression level of CHI3L1 in U-78 MG cells and the addition of this recombinant protein at 2.4 μg/ml attenuated the effect of G721–0282.

In addition, our team also showed inhibition of migration of U-87 MG cells in the scratch assay, which may play a role in the formation of tube-like structures. A similar effect of G721–0282 as a cell migration inhibitor was observed by Park et al. in MG-63 and U2OS osteosarcoma cells [12]. CHI3L1 is well known as a protein that generally plays a stimulatory role in the angiogenesis process, cell migration and also immune modulations that occur in the cancer process. This protein has a broad influence on tumour development and metastasis and therefore inhibition of CHI3L1 may be of potential importance in the development of new targeted therapies and strategies. In glioblastoma, poor prognosis is correlated with high expression of VEGF and CHI3L1 [7]. Previous studies have also shown that CHI3L1 inhibition sensitises glioma cells to radiation [7]. Our research suggests that CHI3L1 inhibition with G721–0282 has a broad spectrum of biological effects, including anti-angiogenesis inhibition, cytokine anti-tumour stimulation and cytoskeletal modulation. Taken together, we conclude that G721–0282 acts as a CHI3L1 inhibitor with potential as a promising agent in the combined treatment of targeted anti-GBM therapy. These studies are an introduction to further research that we intend to conduct on an in vivo model of human glioblastoma to more fully evaluate the clinical utility of anti-cancer therapy involving G721–0282. Any chance of progress in GBM therapy is still valuable and worth exploring and in this work we would like to suggest new additional and possible avenues for further research with potential clinical relevance.

5. Limitation of the study

According to Allen et al., the glioblastoma-like U-87 MG cell is considered to be different from the original human-derived cell line established in 1968 and deposited at the ATCC by J. Ponten [108], but it is still a GBM-derived and well-known cell line model that has been widely used to date. It is also one of the few cell lines, apart from MG-63 and U2OS, that express CHI3L1 and could therefore be used as a model to study the inhibition of this protein.

Funding

This research was partly funded by the Wroclaw Medical University (SUBK.A352.22.033) under the title "The importance of the CHI3L1 protein inhibitor in the inhibition of migration and angiogenesis of glioblastoma cells - in vitro studies" and was carried out by Agnieszka Rusak and statutory funds of the Wroclaw University of Science and Technology (grant number 8211104160).

CRediT authorship contribution statement

AR: Conceptualization. **AR, IB**: Methodology. **AR, IB, MM, BW, MO, KHL, EK, AP, JM**: Investigation. **AR, IB, HP, MPO, PD**: Resources. **AR, IB**: Validation. **AR, IB, AK, KHL**: Visualization. **AR, IB, MM, MO, EK, AP**: Formal analysis. **AR, IB, MM, EK, BW, KHL**: Writing – original draft. **AR, IB, HP, PD**: Writing – review & editing. **MPO, HP, PD**: Supervision. **AR**: Project administration. **AR**: Funding acquisition. All authors have read and agreed to the published version of the manuscript.

Conflict of interest statement

The authors declare that they have no known competing financial

interests or personal relationships that could have appeared to influence the work reported in this paper.

Data availability

Data will be made available on request.

Acknowledgements

The authors would like to thank Magdalena Baran-Pelc and Agnieszka Barańska for excellent technical assistance (Wroclaw Medical University, Wroclaw) and Zdzisław Lewandowski for assistance with visualisation (University Faculty of Physical Education, Wroclaw). The authors are very grateful to Professor Zuzanna Setkowicz-Janeczko from the Laboratory of Experimental Neuropathology, Institute of Biomedical Research, Faculty of Biology, Jagiellonian University (Krakow, Poland) for sharing the IBA1 antibody.

Appendix A. Supporting information

Supplementary data associated with this article can be found in the online version at doi:10.1016/j.biopha.2023.114520.

References

[1] W. Wu, J.L. Klockow, M. Zhang, F. Lafortune, E. Chang, L. Jin, Yang Wu, Glioblastoma Multiforme (GBM): an overview of current therapies and mechanisms of resistance, Pharmacol. Res. 171 (2022) 1–64, https://doi.org/10.1016/j.phrs.2021.105780.

[2] J. Kzhyshkowska, A. Gratchev, S. Goerdt, Human chitinases and chitinase-like proteins as indicators for inflammation and cancer, Biomark. Insights 2 (2007) 128–146.

[3] R. Shao R, K. Hamel, L. Petersen, J. Qing Cao, R.B. Arenas, C. Bigelow, B. Bentley, W. Yan, YKL-40, a secreted glycoprotein, promotes tumor angiogenesis, Oncogene 28 (2009) 4456–4468, https://doi.org/10.1038/onc.2009.292.

[4] G. Steponaitis, D. Skiriutė, A. Kazlauskas, I. Golubickaitė, R. Stakaitis, A. Tamašauskas, P. Vaitkienė, High CHI3L1 expression is associated with glioma patient survival, Diagn. Pathol. 11 (2016) 42, https://doi.org/10.1186/s13000-016-0492-4.

[5] A. Rusak, K. Jabłońska, P. Dzięgiel, Rola białka YKL-40 w procesie nowotworowym/The role of YKL-40 in a cancerous process, Adv. Hyg. Exp. Med. 70 (2016) 1286–1299, https://doi.org/10.5604/17322693.1227353.

[6] T. Zhao, Z. Su, Y. Li, X. Zhang, Q. You, Chitinase-3 like-protein-1 function and its role in diseases, Signal Transduct. Target Ther. 5 (1) (2020) 201, https://doi.org/10.1038/s41392-020-00303-7.

[7] R.A. Francescone, S. Scully, M. Faibish, S.L. Taylor, D. Oh, L. Moral, W. Yan, B. Bentley, R. Shao, Role of YKL-40 in the angiogenesis, radioresistance, and progression of glioblastoma, J. Biol. Chem. 286 (2011) 15332–15343, https://doi.org/10.1074/jbc.M110.212514.

[8] S. Scully, W. Yan, B. Bentley, Q.J. Cao, R. Shao, Inhibitory activity of YKL-40 in mammary epithelial cell differentiation and polarization induced by lactogenic hormones: a role in mammary tissue involution, PLoS One 6 (10) (2011), e25819, https://doi.org/10.1371/journal.pone.0025819.

[9] R. Shao, S.L. Taylor, D.S. Oh, L.M. Schwartz, Vascular heterogeneity and targeting: the role of YKL-40 in glioblastoma vascularization, 1, Oncotarget 6 (38) (2015) 40507–40518, https://doi.org/10.18632/oncotarget.5943.

[10] A. Rusak, K. Jablonska, A. Piotrowska A, et al., The role of CHI3L1 expression in angiogenesis in invasive ductal breast carcinoma, Anticancer Res. 38 (2018) 3357–3366, https://doi.org/10.21873/anticanres.12602.

[11] A. Rusak, K. Jablonska, A. Piotrowska, et al., Correlation of expression of CHI3L1 and Nogo-A and their role in angiogenesis in invasive ductal breast carcinoma, Anticancer Res. 39 (2019) 2341–2350, https://doi.org/10.21873/anticanres.13351.

[12] K.R. Park, H.M. Yun, J.T. Hong, G721-0282 inhibits cell growth and induces apoptosis in human osteosarcoma through down-regulation of the STAT3 pathway, Int. J. Biol. Sci. 16 (2020) 330–341, https://doi.org/10.7150/ijbs.37781.

[13] E. Lionta, G. Spyrou, D. Vassilatis, Z. Cournia, Structure-based virtual screening for drug discovery: principles, applications and recent advances, Curr. Top. Med. Chem. 14 (2014) 1923–1938, https://doi.org/10.2174/1568026614666140929124445.

[14] C.A. Lipinski, F. Lombardo, B.W. Dominy, P.J. Feeney, Experimental and computational approaches to estimate solubility and permeability in drug discovery and development settings, Adv. Drug Deliv. Rev. 46 (2001) 3–26, https://doi.org/10.1016/S0169-409X(00)00129-0.

[15] J.Y. Choi, I.J. Yeo, K.C. Kim, W.R. Choi, J.K. Jung, S.B. Han, J.T. Hong, K284-6111 prevents the amyloid beta-induced neuroinflammation and impairment of recognition memory through inhibition of NF-KB-mediated CHI3L1 expression, J. Neuroinflamm. 15 (2018) 1–13, https://doi.org/10.1186/s12974-018-1269-3.

[16] Ł. Zadka, I. Buzalewicz, A. Ulatowska-Jarża, A. Rusak, M. Kochel, I. Ceremuga, P. Dziegiel, Label-free quantitative phase imaging reveals spatial heterogeneity of extracellular vesicles in select colon disorders, Am. J. Pathol. 191 (2021) 2147–2171, https://doi.org/10.1016/J.AJPATH.2021.08.005.

[17] C.J. Koo, S.E. Jang, S. Park, Y.K. Park, Reconstructed three-dimensional images and parameters of individual erythrocytes using optical diffraction tomography microscopy, Ann. Lab. Med. Seoul. Natl. Univ. Inst. Cogn. Sci. (2019) 223–226, https://doi.org/10.3343/alm.2019.39.2.223.

[18] Y.K. Yang, S.A. Yoon, J. Kim, K. Park, Measurements of Morphological and Biophysical Alterations in Individual Neuron Cells Associated with Early Neurotoxic Effects in Parkinson's Disease, in: Cytom. Part A, 91, Wiley-Liss Inc, 2017, pp. 510–518, https://doi.org/10.1002/cyto.a.23110.

[19] Y.K. Lee, K.R. Kim, K. Jung, J. Heo, J.H. Cho, S. Lee, S. Chang, G. Jo, Y.J. Park, H. Park, Quantitative phase imaging techniques for the study of cell pathophysiology: from principles to applications, Sensors 13 (2013) 4170–4191, https://doi.org/10.3390/s130404170.

[20] Y. Kim, K. Lee, S. Yoon, J. Heo, J. Choi, C. Park, Three-dimensional label-free imaging and quantification of lipid droplets in live hepatocytes, Sci. Rep. 6 (2016) 1–8, https://doi.org/10.1038/srep36815.

[21] T.-K. Kim, B.-W. Lee, F. Fujii, K.-H. Lee, S. Lee, Y. Park, J.K. Kim, S.-W. Lee, C.-G. Pack, Mitotic Chromosomes in Live Cells Characterized Using High-Speed and Label-Free Optical Diffraction Tomography 8 (2019) 1368, https://doi.org/10.3390/cells8111368.

[22] M. Baczewska, K. Eder, S. Ketelhut, B. Kemper, M. Kujawińska, Refractive index changes of cells and cellular compartments upon paraformaldehyde fixation acquired by tomographic phase microscopy, Cytom. Part A (2021) 388–398, https://doi.org/10.1002/cyto.a.24229.

[23] J. Oh, J.S. Ryu, M. Lee, J. Jung, S. Han, H. J.Chung, Y. Park, Three-dimensional label-free observation of individual bacteria upon antibiotic treatment using optical diffraction tomography, Biomed. Opt. Express 11 (2020) 1257, https://doi.org/10.1364/boe.377740.

[24] I. Buzalewicz, A. Ulatowska-Jarża, A. Kaczorowska, M. Gąsior-Głogowska, H. Podbielska, M. Karwańska, A. Wieliczko, A.K. Matczuk, K. Kowal, M. Kopaczyńska, Bacteria single-cell and photosensitizer interaction revealed by quantitative phase imaging, Int. J. Mol. Sci. 22 (2021) 5068, https://doi.org/10.3390/IJMS22105068.

[25] I. Buzalewicz, I. Hołowacz, A.K. Matczuk, M. Guźniczak, D. Skrzela, M. Karwańska, A. Wieliczko, K. Kowal, A. Ulatowska-Jarża, Photolon nanoporous photoactive material with antibacterial activity and label-free noncontact method for free radical detection, Int. J. Mol. Sci. 23 (2022) 279, https://doi.org/10.3390/IJMS23010279.

[26] Ł. Zadka, K. Chrabaszcz, I. Buzalewicz, E. Wiercigroch, N. Glatzel-Plucińska, Ł. Szleszkowski, A. Gomułkiewicz, A. Piotrowska, K. Kurnol, P. Dzięgiel, T. Jurek, K. Malek, Molecular profiling of the intestinal mucosa and immune cells of the colon by multi-parametric histological techniques, Sci. Rep. 11 (2021) 1–16, https://doi.org/10.1038/s41598-021-90761-y.

[27] Y. Sung, W. Choi, C. Fang-Yen, K. Badizadegan, R.R. Dasari, M.S. Feld, Optical diffraction tomography for high resolution live cell imaging, Opt. Express 17 (2009) 266, https://doi.org/10.1364/oe.17.000266.

[28] A. Marian, C. Depeursinge, E. Cuche, F. Charrière, F. Montfort, J. Kuehn, P. Marquet, T. Colomb, Cell refractive index tomography by digital holographic microscopy, Opt. Lett. 31 (2006) 178–180, https://doi.org/10.1364/OL.31.000178.

[29] J. Beuthan, O. Minet, J. Helfmann, M. Herrig, G. Müller, The spatial variation of the refractive index in biological cells, Phys. Med. Biol. 41 (1996) 369, https://doi.org/10.1088/0031-9155/41/3/002.

[30] B. Rappaz, C. Depeursinge, E.A.D. Mitchell, F. Charrière, N. Pavillon, P. Marquet, T.J. Heger, T. Colomb, Living specimen tomography by digital holographic microscopy: morphometry of testate amoeba, Opt. Express 14 (2006) 7005–7013, https://doi.org/10.1364/OE.14.007005.

[31] R. Kaliszan, M. Markuszewski, Brain/blood distribution described by a combination of partition coefficient and molecular mass, Int. J. Pharm. 145 (1996) 9–16, https://doi.org/10.1016/S0378-5173(96)04712-6.

[32] K. Stepnik, W. Kukula-Koch, In silico studies on triterpenoid saponins permeation through the blood–brain barrier combined with postmortem research on the brain tissues of mice affected by astragaloside iv administration, Int. J. Mol. Sci. (2020) 21, https://doi.org/10.3390/ijms21072534.

[33] P. Garg. Drug Absorption Studies, first ed, Springer, New York, 2008, https://doi.org/10.1007/978-0-387-74901-3.

[34] M.H. Abraham, A. Ibrahim, A.M. Zissimos, Y.H. Zhao, J. Comer, D.P. Reynolds, Application of hydrogen bonding calculations in property based drug design, Drug Discov. Today 7 (2002) 1056–1063, https://doi.org/10.1016/S1359-6446(02)02478-9.

[35] M. Janicka, M. Sztanke, K. Sztanke, Predicting the blood-brain barrier permeability of new drug-like compounds via HPLC with various stationary phases, Molecules (2020) 25, https://doi.org/10.3390/molecules25030487.

[36] C.W. Yap, PaDEL-descriptor: an open source software to calculate molecular descriptors and fingerprints, J. Comput. Chem. 32 (2011) 1466–1474, https://doi.org/10.1002/jcc.21707.

[37] K. Balon, B. Wiatrak, PC12 and THP-1 cell lines as neuronal and microglia model in neurobiological research, Appl. Sci. 11 (2021) 3729, https://doi.org/10.3390/app11093729.

[38] J. Korbecki, I. Gutowska, M. Wiercioch, A. Łukomska, M. Tarnowski, A. Drozd, K. Barczak, D. Chlubek, I. Baranowska-Bosiacka, Sodium orthovanadate changes

fatty acid composition and increased expression of stearoyl-coenzyme a desaturase in thp-1 macrophages, Biol. Trace Elem. Res. 193 (2020) 152–161, https://doi.org/10.1007/s12011-019-01699-2.
[39] P. Skehan, R. Storeng, D. Scudiero, A. Monks, J. Mcmahon, D. Vistica, J. T. Warren, H. Bokesch, S. Kenney, M.R. Boyd, New colorimetric cytotoxicity assay for anticancer-drug screening, J. Natl. Cancer Inst. 82 (1990) 1107–1112, https://doi.org/10.1093/jnci/82.13.1107.
[40] E.A. Orellana, A.L. Kasinski, Sulforhodamine B (SRB) assay in cell culture to investigate cell proliferation, Bio Protoc. 6 (21) (2016) 1–12, https://doi.org/10.21769/BioProtoc.1984.
[41] K. Ratajczak K, N. Glatzel-Plucińska, K. Ratajczak-Wielgomas, K. Nowińska, S. Borska, Effect of resveratrol treatment on human pancreatic cancer cells through alterations of Bcl-2 family members, Molecules 26 (2021) 1–21, https://doi.org/10.3390/molecules26216560.
[42] K. Solarska-Ściuk, K. Adach, M. Fijałkowski, K. Haczkiewicz-Leśniak, M. Kulus, M. Olbromski, N. Glatzel-Plucińska, O. Szelest, D. Bonarska-Kujawa, Identifying the molecular mechanisms and types of cell death induced by bio- and pyr-silica nanoparticles in endothelial cells, Int. J. Mol. Sci. 23 (2022) 5103, https://doi.org/10.3390/ ijms23095103.
[43] R.A. Francescone III, M. Faibish, R. Shao, A matrigel-based tube formation assay to assess the vasculogenic activity of tumor cells, J. Vis. Exp. (2011) 552–555, https://doi.org/10.3791/3040.
[44] P. Nowak-Śliwińska, K. Alitalo, E. Allen, et al., Consensus guidelines for the use and interpretation of angiogenesis assays, Angiogenesis 21 (3) (2018) 425–532, https://doi.org/10.1007/s10456-018-9613-x.
[45] G. Cory, Scratch-wound assay, Methods Mol. Biol. 769 (2011) 25–30, https://doi.org/10.1007/978-1-61779-207-6_2.
[46] E.M. Alishahedani, M. Yadav, K.J. McCann, P. Gough, C.R. Castillo, J. Matriz, I. A. Myles, Therapeutic candidates for keloid scars identified by qualitative review of scratch assay research for wound healing, PLoS One 16 (6) (2021) 1–32. ⟨https://doi.org/10.1371/journal.pone.0253669⟩.
[47] T. Machałowski, A. Rusak, B. Wiatrak, K. Haczkiewicz-Leśniak, A. Popiel, J. Jaroszewicz, A. Żak, M. Podhorska-Okołów, T. Jesionowski, Naturally formed chitinous skeleton isolated from the marine demosponge Aplysina fistularis as a 3d scaffold for tissue engineering, Materials (2021) 14, https://doi.org/10.3390/ma14112992.
[48] A.M. Kmiecik, B. Pula, J. Suchanski, M. Olbromski, A. Gomulkiewicz, T. Owczarek, A. Kruczak, A. Ambicka, J. Rys, M. Ugorski, M. Podhorska-Okolow, P. Dziegiel, Metallothionein-3 increases triple-negative breast cancer cell invasiveness via induction of metalloproteinase expression, PLoS One 10 (5) (2015) 1–25, https://doi.org/10.1371/journal.pone.0124865.
[49] M. Cabeza-Segura, V. Gambardella, F. Gimeno-Valiente, et al., Integrative immune transcriptomic classification improves patient selection for precision immunotherapy in advanced gastro-oesophageal adenocarcinoma, Br. J. Cancer 127 (2022) 2198–2206, https://doi.org/10.1038/s41416-022-02005-z.
[50] P.P.G. Mulder, M. Vlig, B.K.H.L. Boekema, et al., Persistent systemic inflammation in patients with severe burn injury is accompanied by influx of immature neutrophils and shifts in t cell subsets and cytokine profiles, Front. Immunol. 11 (2021), 621222, https://doi.org/10.3389/fimmu.2020.621222 eCollection 2020.
[51] K. Muguruma, A. Nishiyama, H. Kawakami, K. Hashimoto, Y. Sasai, Self-organization of polarized cerebellar tissue in 3d culture of human pluripotent stem cells, Cell Rep. 10 (4) (2015) 537–550. ⟨https://doi.org/10.1016/j.celrep.2014.12.051⟩.
[52] Y. Bamba, T. Shofuda, D. Kanematsu, M. Nonaka, M. Yamasaki, H. Okano, Y. Kanemura, Differentiation, polarization, and migration of human induced pluripotent stem cell-derived neural progenitor cells co-cultured with a human glial cell line with radial glial-like characteristics, Biochem. Biophys. Res. Commun. 447 (4) (2014) 683–688, https://doi.org/10.1016/j.bbrc.2014.04.070.
[53] A. Amann, M. Zwierzina, S. Koeck, G. Gamerith, E. Pechriggl, J.M. Huber, E. Lorenz, J.M. Kelm, W. Hilbe, H. Zwierzina, J. Kern, Development of a 3D angiogenesis model to study tumour - endothelial cell interactions and the effects of anti-angiogenic drugs, 71-13, Sci. Rep. (2017), https://doi.org/10.1038/s41598-017-03010-6.
[54] M. Olbromski, J. Grzegrzółka, A. Jankowska-Konsur, W. Witkiewicz, M. Podhorska-Okołów, P. Dzięgiel, MicroRNAs modulate the expression of the SOX18 transcript in lung squamous cell carcinoma, Oncol. Rep. (2016) 362884–362892, https://doi.org/10.3892/or.2016.5102.
[55] A. Popiel-Kopaczyk, J. Grzegrzółka, A. Piotrowska, et al., The expression of testin, Ki-67 and p16 in cervical cancer diagnostics, Curr. Issues Mol. Biol. 45 (1) (2023) 490–500, https://doi.org/doi::10.3390/cimb45010032.
[56] M. Wissel, M. Poirier, C. Satterwhite, et al., Recommendations on qPCR/ddPCR assay validation by GCC, Bioanalysis 14 (12) (2022) 853–863, https://doi.org/doi: 10.4155/bio-2022-0109.
[57] U.K. Laemmli, Cleavage of structural proteins during the assembly of the head of bacteriophage T4, Nature 227 (1970) 680–685, https://doi.org/10.1038/227680a0.
[58] C. Cotte, Y. Toy, F. Jourdain, P. Pavillon, N. Boss, D. Magistretti, P. Marquet, P. Depeursinge, Marker-free phase nanoscopy, Nat. Photonics 7 (2013) 113–117, https://doi.org/10.1038/nphoton.2012.329.
[59] Y. Shin, S. Kim, D. Kim, K. Park, Super-resolution three-dimensional fluorescence and optical diffraction tomography of live cells using structured illumination generated by a digital micromirror device, Sci. Rep. 8 (2018) 1–8, https://doi.org/10.1038/s41598-018-27399-w.
[60] R. Barer, Interference microscopy and mass determination, Nature 169 (1952) 366–367, https://doi.org/10.1038/169366b0.
[61] M. Friebel, M. Meinke, Model function to calculate the refractive index of native hemoglobin in the wavelength range of 250-1100 nm dependent on concentration, Appl. Opt. 45 (2006) 2838–2842, https://doi.org/10.1364/AO.45.002838.
[62] O.J.T. Phillips, K.G. Jacques, S.L. McCarty, Measurement of single cell refractive index, dry mass, volume, and density using a transillumination microscope, Phys. Rev. Lett. (2012) 109, https://doi.org/10.1117/1.jbo.20.12.126009.
[63] S. Aknoun, J. Savatier, P. Bon, F. Galland, L. Abdeladim, B. Wattellier, S. Monneret, Living cell dry mass measurement using quantitative phase imaging with quadriwave lateral shearing interferometry: an accuracy and sensitivity discussion, J. Biomed. Opt. 20 (2015), 126009, https://doi.org/10.1117/1.JBO.20.12.126009.
[64] S. Kunwittaya, C. Nantasenamat, L. Treeratanapiboon, A. Srisarin, Influence of logBB cut-off on the prediction of blood-brain barrier permeability, Biomed. Appl. Technol. J. 1 (2013) 16–34.
[65] C.S. Vilar, S. Chakrabarti, Prediction of passive blood-brain partitioning: straightforward and effective classification models based on in silico derived physicochemical descriptor, J. Mol. Graph Model 28 (2010) 899–903, https://doi.org/10.1016/j.jmgm.2010.03.010.
[66] S. Giraud, B. Bessette, C. Boda, F. Lalloué, D. Petit, M. Mathonnet, M.-O. Jauberteau, In vitro apoptotic induction of human glioblastoma cells by Fas ligand plus etoposide and in vivo antitumour activity of combined drugs in xenografted nude rats, Int. J. Oncol. 30 (2007) 273–281, https://doi.org/10.3892/ijo.30.1.273.
[67] B. Gul, S. Ashraf, S. Khan, H. Nisar, I. Ahmad, Cell refractive index: models, insights, applications and future perspectives, Photodiagn. Photodyn. Ther. (2021) 33, https://doi.org/10.1016/j.pdpdt.2020.102096.
[68] H.J. Ham, Y.S. Lee, H.P. Lee, Y.W. Ham, J. Yun, G721-0282 Exerts Anxiolytic-Like Effects on Chronic Unpredictable Mild Stress in Mice Through Inhibition of Chitinase-3-Like 1-Mediated Neuroinflammation 16 (2022) 1–14, https://doi.org/10.1111/bph.15308.
[69] S.S. Widodo, M. Dinevska, L.M. Furst, S.S. Stylli, T. Mantamadiotis, IL-10 in glioma, Br. J. Cancer 125 (2021) 1466–1476, https://doi.org/10.1038/s41416-021-01515-6.
[70] M. Bartak, M. Chodkowski, A. Słońska, M. Grodzik, J. Szczepaniak, M. W. Bańbura, J. Cymerys, Equid alphaherpesvirus 1 modulates actin cytoskeleton and inhibits migration of glioblastoma multiforme cell line A172, Pathogens 11 (2022) 400, https://doi.org/10.3390/pathogens11040400.
[71] P.T. Bozza, J.P.B. Viola, Lipid droplets in inflammation and cancer, Prostaglandins Leukot. Essent. Fat. Acids (82 (2010) 243–250, https://doi.org/10.1016/j.plefa.2010.02.005.
[72] M.A. Welte, Proteins under new management: lipid droplets deliver, Trends Cell Biol. 17 (2007) 363–369, https://doi.org/10.1016/J.TCB.2007.06.004.
[73] T. Jarc, E. Petan, Focus: organelles: lipid droplets and the management of cellular stress, Yale J. Biol. Med. 92 (3) (2019) 435–452.
[74] A.S. Greenberg, R.A. Coleman, F.B. Kraemer, J.L. McManaman, M.S. Obin, V. Puri, Q.W. Yan, H. Miyoshi, D.G. Mashek, The role of lipid droplets in metabolic disease in rodents and humans, J. Clin. Invest. 121 (2011) 2102–2110, https://doi.org/10.1172/jci46069.
[75] J.A. Olzmann, P. Carvalho, Dynamics and functions of lipid droplets, Nat. Rev. Mol. Cell Biol. 20 (2018) 137–155, https://doi.org/10.1038/s41580-018-0085-z.
[76] S. Martin, R.G. Parton, Lipid droplets: a unified view of a dynamic organelle, Nat. Rev. Mol. Cell Biol. 7 (2006) 373–378, https://doi.org/10.1038/nrm1912.
[77] A.L.S. Cruz, E. de, A. Barreto, N.P.B. Fazolini, J.P.B. Viola, P.T. Bozza, Lipid droplets: platforms with multiple functions in cancer hallmarks, Cell Death Dis. (2020) 11, https://doi.org/10.1038/s41419-020-2297-3.
[78] M. Maan, J.M. Peters, M. Dutta, A.D. Patterson, Lipid metabolism and lipophagy in cancer, Biochem. Biophys. Res. Commun. 504 (2018) 582–589, https://doi.org/10.1016/j.bbrc.2018.02.097.
[79] G.D. Geng F, X. Cheng, X. Wu, J.Y. Yoo, C. Cheng, J.Y. Guo, X. Mo, P. Ru, B. Hurwitz, S.H. Kim, J. Otero, V. Puduvalli, E. Lefai, J. Ma, I. Nakano, C. Horbinski, B. Kaur, A. Chakravarti, Inhibition of SOAT1 suppresses glioblastoma growth via blocking SREBP-1-mediated lipogenesis, Clin. Cancer Res. 22 (2016) 5337–5348, https://doi.org/10.1158/1078-0432.CCR-15-2973.
[80] L. Tong, C. Xie, Y. Wei, Y. Qu, H. Liang, Y. Zhang, Antitumor Effects of Berberine on Gliomas via Inactivation of Caspase-1-Mediated IL-1 β and IL-18 Release 9 (2019) 1–13, https://doi.org/10.3389/fonc.2019.00364.
[81] K. Kai, Y. Komohara, S. Esumi, Y. Fujiwara, T. Yamamoto, K. Uekawa, Macrophage/microglia - derived IL - 1β induces glioblastoma growth via the STAT3 / NF - κB pathway, Hum. Cell 35 (2022) 226–237, https://doi.org/10.1007/s13577-021-00619-8.
[82] Y. Shan, X. He, W. Song, D. Han, J. Niu, J. Wang, Role of IL-6 in the invasiveness and prognosis of glioma, Int. J. Clin. Exp. Med. 8 (2015) 9114–9120.
[83] F. Yang, Z. He, H. Duan, D. Zhang, J. Li, H. Yang, J.F. Dorsey, W. Zou, S. A. Nabavizadeh, S.J. Bagley, K. Abdullah, S. Brem, L. Zhang, X. Xu, K.T. Byrne, R. H. Vonderheide, Y. Gong, Y. Fan, Synergistic immunotherapy of glioblastoma by dual targeting of IL-6 and CD40, Nat. Commun. (2021) 1–15, https://doi.org/10.1038/s41467-021-23832-3.
[84] Huang, et al., Immunomodulatory effects and potential clinical applications of dimethyl sulfoxide, Immunobiology 225 (2020), 151906, https://doi.org/10.1016/j.imbio.2020.151906.
[85] Lin, et al., Dimethyl sulfoxide inhibits spontaneous diabetes and autoimmune recurrence in non-obese diabetic mice by inducing differentiation of regulatory T cells, Toxicol. Appl. Pharmacol. 282 (2015) 207–214, https://doi.org/10.1016/j.taap.2014.11.012 0041-008X.

[86] F. Ahangari, A. Sood, B. Ma, S. Takyar, M. Schuyler, C. Qualls, C.S. Dela Cruz, G. L. Chupp, C.G. Lee, Chitinase 3 – like-1 regulates both visceral fat accumulation and, Am. J. Respir. Crit. Care Med. 191 (2015) 746–757, https://doi.org/10.1164/rccm.201405-0796OC.
[87] K. Gabrusiewicz, A. Ellert-Miklaszewska, M. Lipko, M. Sielska, B. Kaminska, Characteristics of the alternative phenotype of microglia / macrophages and its modulation in experimental gliomas, PLoS One 6 (2011) 1–12, https://doi.org/10.1371/journal.pone.0023902.
[88] L. Zadka, P. Kram P, J. Koscinski, R. Jankowski, M. Kaczmarek, K. Piatek, M. Kulus, A. Gomulkiewicz, A. Piotrowska, P. Dziegiel, Association between interleukin-10 receptors and the cd45-immunophenotype of central nervous system tumors: a preliminary study, Anticancer Res 37 (2017) 5777–5783, https://doi.org/10.21873/anticanres.12019.
[89] M. Saraiva, P. Vieira, A.O. Garra, Biology and therapeutic potential of interleukin-10, J. Exp. Med. (2019) 1–19, https://doi.org/10.1084/jem.20190418.
[90] K. Yasuda, K. Nakanishi, H. Tsutsui, Interleukin-18 in health and disease, Int. J. Mol. Sci. 20 (2019) 1–54, https://doi.org/10.3390/ijms20030649.
[91] Z. Ma, W. Li, S. Yoshiya, Y. Xu, M. Hata, Y. El-darawish, T. Markova, K. Yamanishi, H. Yamanishi, H. Tahara, Augmentation of Immune checkpoint cancer immunotherapy with IL18, Clin. Cancer Res. 22 (2016) 2969–2980, https://doi.org/10.1158/1078-0432.CCR-15-1655.
[92] A. Kunert, M. Chmielewski, R. Wijers, C. Berrevoets, H. Abken, R. Debets, Intratumoral production of IL18, but not IL12, by TCR-engineered T cells is non-toxic and counteracts immune evasion of solid tumors, Oncoimmunology 7 (2018) 1–12, https://doi.org/10.1080/2162402X.2017.1378842.
[93] M.J. Robertson, J.W. Mier, T. Logan, M. Atkins, H. Koon, K.M. Koch, S. Kathman, L.N. Pandite, C. Oei, L.C. Kirby, R.C. Jewell, W.N. Bell, L.M. Thurmond, J. Weisenbach, S. Roberts, M.M. Dar, Cancer Therapy: Clinical Clinical and Biological Effects of Recombinant Human Interleukin-18 Administered by Intravenous Infusion to Patients with Advanced Cancer 12 (2006) 4265–4273, https://doi.org/10.1158/1078-0432.CCR-06-0121.
[94] S. Park, S. Cheon, D. Cho, The dual effects of interleukin-18 in tumor progression, Cell. Mol. Immunol. Rev. 4 (5) (2007) 329–335.
[95] O.T. Kikuchi T, Y. Akasaki, T. Joki, T. Abe, M. Kurimoto, Antitumor activity of interleukin-18 on mouse glioma cells, J. Immunother. 23 (2000) 184–189, https://doi.org/10.1097/00002371-200003000-00002.
[96] B.L. Salomon, Tumor necrosis factor α and regulatory t cells in oncoimmunology, Front. Immunol. 9 (2018) 1–12, https://doi.org/10.3389/fimmu.2018.00444.
[97] F. Balkwill, Tumour necrosis factor and cancer, Nat. Rev. Cancer 9 (2009) 361–371, https://doi.org/10.1038/nrc2628.
[98] S. Madhusudan, S.R. Muthuramalingam, J.P. Braybrooke, S. Wilner, K. Kaur, C. Han, S. Hoare, F. Balkwill, T.S. Ganesan, Study of etanercept, a tumor necrosis factor-alpha inhibitor, in recurrent ovarian cancer, J. Clin. Oncol. 23 (2005) 5950–5959, https://doi.org/10.1200/JCO.2005.04.127.
[99] S. Sangaletti, C. Tripodo, C. Ratti, S. Piconese, R. Porcasi, R. Salcedo, G. Trinchieri, M.P. Colombo, Oncogene-driven intrinsic inflammation induces leukocyte production of tumor necrosis factor that critically contributes to mammary carcinogenesis, Cancer Res. 70 (2010) 7764–7775, https://doi.org/10.1158/0008-5472.CAN-10-0471.
[100] M.S. Drutskaya, TNF neutralization results in the Delay of Transplantable Tumor growth and reduced MDSC accumulation, Front. Immunol. 7 (2016) 1–11, https://doi.org/10.3389/fimmu.2016.00147.
[101] M. Uhl, S. Aulwurm, J. Wischhusen, M. Weiler, J.Y. Ma, A.R.R. Mangadu, Y.-W. Liu, M. Platten, U. Herrlinger, A. Murphy, D.H. Wong, W. Wick, L.S. Higgins, M. Weller, SD-208, a novel transforming growth factor beta receptor I kinase inhibitor, inhibits growth and invasiveness and enhances immunogenicity of murine and human glioma cells in vitro and in vivo, Cancer Res. 64 (2004) 7954–7961, https://doi.org/10.1158/0008-5472.CAN-04-1013.
[102] A. Wick, A. Desjardins, C. Suarez, P. Forsyth, I. Gueorguieva, T. Burkholder, Phase 1b/2a study of galunisertib, a small molecule inhibitor of transforming growth factor-beta receptor I, in combination with standard temozolomide-based radiochemotherapy in patients with newly diagnosed malignant glioma, Investig. New Drugs 38 (2020) 1570–1579, https://doi.org/10.1007/s10637-020-00910-9.
[103] A.A. Brandes, A.F. Carpentier, S. Kesari, J.M. Sepulveda-sanchez, H.R. Wheeler, O. Chinot, L. Cher, J.P. Steinbach, D. Capper, P. Specenier, J. Rodon, A. Cleverly, C. Smith, I. Gueorguieva, C. Miles, S.C. Guba, D. Desaiah, M.M. Lahn, W. Wick, A Phase II randomized study of galunisertib monotherapy or galunisertib plus lomustine compared with lomustine monotherapy in patients with recurrent glioblastoma, Neuro-Oncol. 18 (2016) 1146–1156, https://doi.org/10.1093/neuonc/now009.
[104] A. Chen, Y. Jiang, Z. Li, L. Wu, U. Santiago, H. Zou, C. Cai, V. Sharma, Y. Guan, L. H. Mccarl, J. Ma, Y.L. Wu, J. Michel, Y. Shi, L. Konnikova, N.M. Amankulor, P. O. Zinn, G. Kohanbash, S. Agnihotri, S. Lu, et al., Chitinase-3-like 1 protein complexes modulate macrophage-mediated immune suppression in glioblastoma, J. Clin. Invest. 131 (2021) 1–18, https://doi.org/10.1172/JCI147552.
[105] A. Soubéran, A. Tchoghandjian, Practical review on preclinical human 3d glioblastoma models: advances and, Cancers 12 (2020) 1–21, https://doi.org/10.3390/cancers12092347.
[106] A. Musah-Eroje, S. Watson, A novel 3D in vitro model of glioblastoma reveals resistance to temozolomide which was potentiated by hypoxia, J. Neurooncol. 142 (2019) 231–240, https://doi.org/10.1007/s11060-019-03107-0.
[107] A.S. Tatla, A.W. Justin, C. Watts, A.E. Markaki, A vascularized tumoroid model for human glioblastoma angiogenesis, Sci. Rep. (2021) 1–9, https://doi.org/10.1038/s41598-021-98911-y.
[108] M. Allen, M. Bjerke, H. Edlund, S. Nelander, B. Westermark, Origin of the U87MG glioma cell line: good news and bad news, Sci. Transl. Med. 8 (2016) 1–5, https://doi.org/10.1126/scitranslmed.aaf6853.